

# AnoPLe: Few-Shot Anomaly Detection via Bi-directional Prompt Learning with Only Normal Samples

Yujin Lee\* Seoyoon Jang\* Hyunsoo Yoon  
 Department of Industrial Engineering, Yonsei University  
 Seoul, South Korea

{yjlee9040, tjdbbs70002, hs.yoon}@yonsei.ac.kr

## Abstract

Few-shot Anomaly Detection (FAD) poses significant challenges due to the limited availability of training samples and the frequent absence of abnormal samples. Previous approaches often rely on annotations or true abnormal samples to improve detection, but such textual or visual cues are not always accessible. To address this, we introduce AnoPLe, a multi-modal prompt learning method designed for anomaly detection without prior knowledge of anomalies. AnoPLe simulates anomalies and employs bi-directional coupling of textual and visual prompts to facilitate deep interaction between the two modalities. Additionally, we integrate a lightweight decoder with a learnable multi-view signal, trained on multi-scale images to enhance local semantic comprehension. To further improve performance, we align global and local semantics, enriching the image-level understanding of anomalies. The experimental results demonstrate that AnoPLe achieves strong FAD performance, recording 94.1% and 86.2% Image AUROC on MVTEC-AD and VisA respectively, with only around a 1% gap compared to the SoTA, despite not being exposed to true anomalies. Code is available at <https://github.com/YoojLee/AnoPLe>.

## 1. Introduction

In real-world, it is challenging to obtain true abnormal samples and often impractical to secure large amounts of accurately verified normal samples. This challenge has ignited interest in robust few-shot anomaly detection methods [6, 13, 19]. Recently, large-scale vision-language models (VLMs) [9, 17] have shown promise in zero- and few-shot scenarios with proper prompt engineering. Pointing out that prompt engineering is suboptimal and time-consuming, previous works in few-shot image classification [11, 27, 28] have replaced manually engineered hard

\*These authors contributed equally to this work.

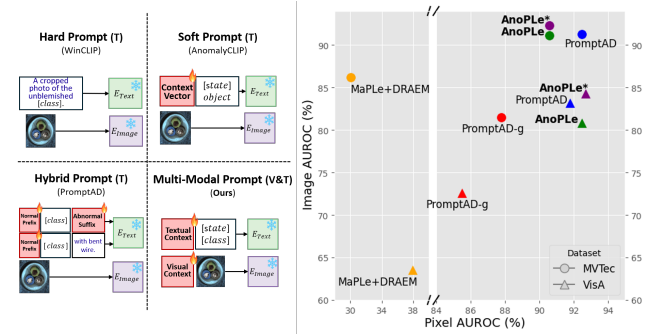


Figure 1. (Left) Different prompt designs used in prompt-guided anomaly detection. (Right) Comparative results in prompt-guided anomaly detection on MVTEC-AD [1] and VisA [31]. PromptAD-g is PromptAD [13] without object customized prompts, while MaPLE+DRAEM combines MaPLE [11] with pseudo anomalies [23]. AnoPLe\* and AnoPLe refer to our method in the one- and multi-class settings, respectively.

prompts with learnable continuous vectors. Similarly, in recent years, there has been active research on CLIP-based zero- and few-shot methods within the domain of anomaly detection. Pioneering work [8] in the CLIP-based methods used manually engineered prompts for anomaly detection, followed by subsequent works based on learnable prompts.

While introducing learnable context vectors rather than solely relying on hard prompts, recent studies based on prompt learning are, to some extent, not completely free from pre-defined knowledge. Several works require true anomalous images as an auxiliary dataset during training [29, 30], or inject prior domain expertise regarding anomalies within text prompts [2, 14]. For example, PromptAD [13] combines both hard and soft prompts, using hard prompts with prior knowledge about object-customized anomalies (e.g., zipper with broken fabric) as a guide to align the soft prompts during training (Fig. 1). Although these methods have shown remarkable performance in few-shot scenarios than prompt engineering, it is not guaranteed

to prior knowledge of abnormality is always available.

Thus, assuming no prior information about abnormal data in either visual or textual aspects, we aim to detect anomalies using only few normal images. To achieve this, we simulate anomalies to prompt CLIP [17] to distinguish between normal and abnormal samples. In Figure 1, we provide generic prompts to the text encoder (e.g., “abnormal”)<sup>1</sup>. Additionally, to maximize the use of coarse information about abnormalities from simulated anomalies, we feed visual contexts into the image encoder.

Given the limited information from textual or visual inputs alone, we promote interaction between these contexts to better capture anomalies in CLIP’s representation space. Unlike clear labels in image classification, the concept of “abnormal” is vague in CLIP, making textual context less informative. Therefore, conditioning the visual context solely on textual context can be suboptimal. To address this, we propose “**AnoPLe**,” a bidirectional prompt learning approach where textual context also references visual context enabling effective few-shot AD without relying on predefined textual or visual semantics about anomalous samples.

Specifically, as shown in Figure 1, when compared with methods without prior knowledge on genuine anomalies, we outperform baselines with significant margin - MaPLe [11] with pseudo anomalies following DRAEM [23] and PromptAD-g which indicates PromptAD [13] relies only on generic prompts. Furthermore, despite using highly generic prompts in a multi-class setting, AnoPLe achieves Image-AUROC comparable to PromptAD [13], the state-of-the-art (SoTA) method, leveraging prior knowledge of anomalies. As we extend our model to the one-class-one-model setting (AnoPLe\*), we surpass PromptAD[13] even without any prior knowledge.

In anomaly detection, it is crucial to localize the anomalous regions as well. However, CLIP struggles with capturing local semantics. Hence, previous studies have addressed this by sliding windows to focus on local regions, which increases computational load and slows down inference times [8], or by modifying the QKV self-attention with value-to-value (V-V) attention to enhance fine-grained details [13, 29]. However, V-V attention may be incompatible with multi-modal prompting, as it modifies the visual representation space, potentially compromising the capture of accurate local semantics.

Therefore, inspired by MaskCLIP [26], we introduce a light-weight decoder to decode the CLIP’s patch features for localization. To improve localization, we feed additional sub-images along with the original image, without overlapping patches. We only use the original image during testing, which causes a distributional shift. To address this, we train the model to recognize whether an image is a sub-image

<sup>1</sup>Since our textual prompts are not bounded to the type of objects, AnoPLe operates in multi-class setting as [22].

or not, mitigating the shift’s impact. In anomaly detection, localization results often inform image-level anomaly detection [18, 22], so we distill pixel-level information into image-level representations to enhance anomaly detection performance at the image-level.

Given that prior knowledge about anomalies is unavailable, AnoPLe shows robust performance in few-shot AD tasks by leveraging strong coupling of multi-modal prompts and a lightweight decoder. Experimental results highlight our strong performance, achieving 94.1% I-AUROC in the 1-shot and 96.3% in the 4-shot settings on MVTec [1], and a competitive 86.2% I-AUROC in the 1-shot scenario on VisA [31]. These results demonstrate that AnoPLe performs on par with the current SoTA [13], without relying on textual descriptions of anomalies. Our contribution is summarized as:

- We introduce a multi-modal prompting approach for few-shot anomaly detection, using simulated anomalies and modality interaction, representing a novel application of deep prompts in CLIP-based anomaly detection.
- We improve anomaly localization with a lightweight decoder that learns local semantics from multiple view and distills pixel-level knowledge into global representations.
- AnoPLe achieves strong few-shot anomaly detection performance with 94.1% and 86.2% of I-AUROC in MVTec and VisA respectively, which is just around 1% gap compared to the SoTA without exposure to true anomalies.

## 2. Related work

### 2.1. Few-Shot Anomaly Detection

Few-shot Anomaly Detection aims to train models that generalize well with only a few normal samples. Previous studies in this area have mainly focused on few-shot transfer, where the model is trained on the entire given dataset or set of classes and then transferred to the target dataset or classes with only a few samples [5, 6]. Notably, RegAD [6] performs class transfer with few-shot learning, leveraging pre-learned features from different classes during the training process. AnomalyGPT [5] utilizes auxiliary datasets to learn prompts in a fully supervised manner to facilitate unsupervised learning and conducts inference through in-context learning. Several studies propose learning abnormalities using only a few normal images without any explicit exposure to the domain of anomaly detection [8, 13, 18]. These approaches are more challenging than few-shot transfer, as the model must learn representations for anomaly detection with only a few images. In this work, we follow the latter settings since they are closer to real-world situations.

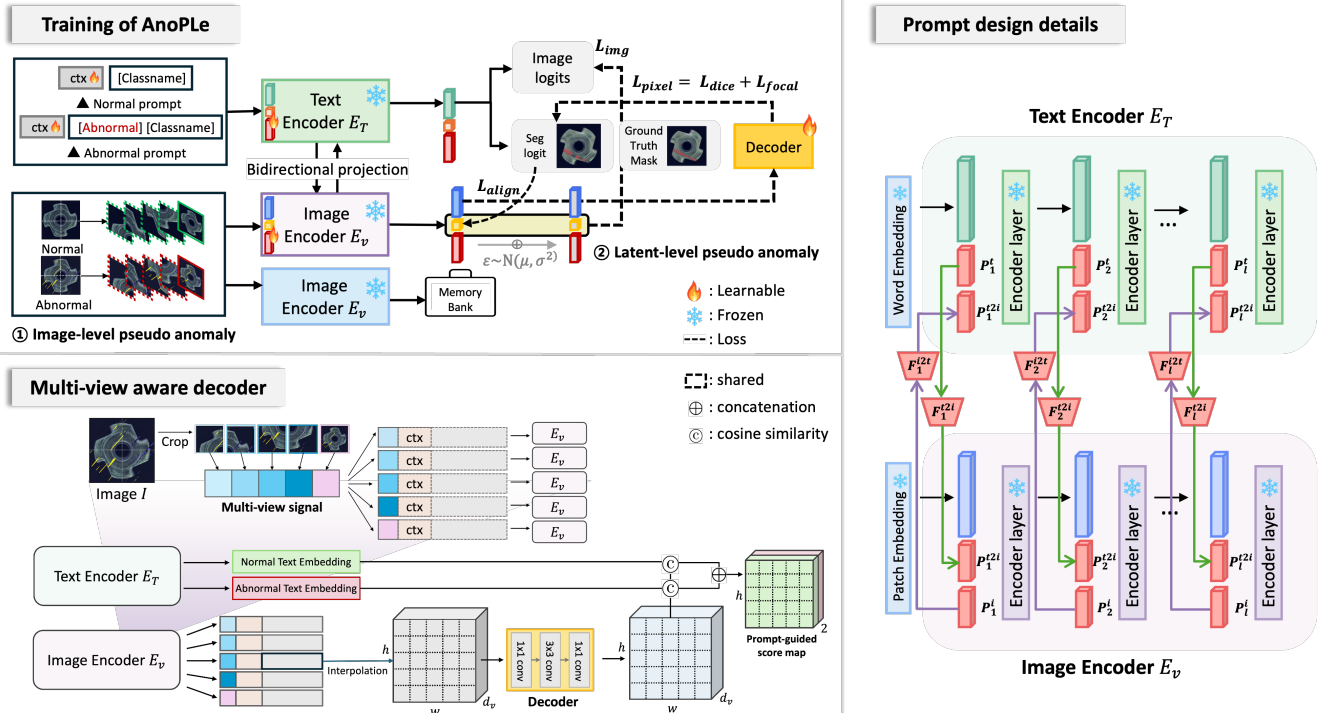


Figure 2. **Overview of AnoPLe.** AnoPLe leverages learnable multi-modal deep prompts with bidirectional coupling between textual and visual prompts, utilizing pseudo anomalies. For localization, we introduce a multi-view aware decoder, enabling the model to effectively learn both local and global anomalies. During training, prompts are updated through local/global level losses and an alignment loss. During inference, the anomaly score is derived from prediction logits and a visual memory bank.

## 2.2. Prompting VLMs for Anomaly Detection

VLMs [9, 17] have been actively discussed within the AD domain as well. Some studies retain the original textual representation space from CLIP [17] and adjust the encoder’s output by leveraging an adapter following the encoder [2, 5, 30]. InCTRL [30] trains the model to be aware of discrepancies between query images and few-shot normal sample prompts through in-context residual learning, sampling query images from true anomalous data. AnoVL [2] conducts prompt engineering for textual inputs and adjusts visual representation with the subsequent adapter. AnomalyGPT [5] feeds learnable prompts as visual input into large VLMs [20] and incorporates textual descriptions with tailored anomaly information for each class.

Another widespread approach is to prepend context vectors to the inputs of the encoder, adjusting the representation of token embeddings during the forward pass [13, 29]. AnomalyCLIP [29] explores the feasibility of textual deep learnable prompts in zero-shot transfer after learning abnormalities from true anomalous samples. Meanwhile, PromptAD [13] does not utilize abnormal images but still requires textual descriptions for each object in abnormal states. In contrast, our approach demonstrates favorable performance

by excluding visual or textual cues of true anomalies and strongly coupling context vectors prepended to both the image and text encoders.

## 3. Method

### 3.1. Overview

AnoPLe aims to detect anomalies using only few normal images without any cues on true anomalies. To achieve this, we simulate anomalies both in pixel and latent space following [23] and [16], respectively. Here, the visual encoder  $E_V$  processes both normal ( $I^+$ ) and simulated abnormal images ( $I^-$ ). Given that pseudo anomalies are not as informative as true anomalies, it is suboptimal to have learnable contexts propagate through just a single branch. Thus, we introduce learnable prompts within both visual and textual encoder ( $E_V, E_T$ ) and encourage a strong coupling between modalities. Specifically, prompts from each modality are projected to the other’s hidden dimension and concatenated with the original prompts.

To enhance anomaly localization, we introduce a multi-view aware lightweight decoder  $D$ . During training,  $N$  sub-images are fed along with the original image  $I_0$  to bootstrap local semantics knowledge from CLIP. At inference, only

the original image  $I_0$  is used to reduce computational overhead. This might lead to potential distributional shift. To mitigate this, a multi-view signal is prepended to the visual prompts, enabling the model to distinguish an original view of the image from sub-images. Furthermore, we align global semantics of the encoder with local semantics to enhance image-level anomaly detection.

## 3.2. Multi-Modal Prompts for Anomaly Detection

### 3.2.1 Textual and Visual Prompt Learning

In this section, we provide brief preliminaries for prompt learning and how we construct the initial state of prompts for each modalities.

For textual prompting, Text Encoder  $E_T$  takes a word embedding  $e_0$  as an input. The textual input  $\mathbf{e}_0^+$  and  $\mathbf{e}_0^-$  for normal and abnormal text prompts are defined as:

$$\mathbf{e}_0^+ = [class], \quad \mathbf{e}_0^- = [abnormal][class], \quad (1)$$

respectively.  $[class]$  refers to the name of each class. Note that we inject abnormalities via textual prompts (i.e., a mere word embedding of “abnormal”) as minimal as possible.

Then, learnable textual context vectors  $\mathbf{P}_0^t \in \mathbb{R}^{C_t \times d_t}$ , where  $C_t$  and  $d_t$  indicates a length of context vectors and hidden dimension of  $E_T$ , are prepended to  $\mathbf{e}_0$ . For the input to  $E_T$ , we define:

$$\mathbf{w}_0^+ = [\mathbf{P}_0^t, \mathbf{e}_0^+], \quad \mathbf{w}_0^- = [\mathbf{P}_0^t, \mathbf{e}_0^-], \quad (2)$$

where  $\mathbf{w}_0^+$ ,  $\mathbf{w}_0^-$  refers to normal and abnormal textual features. We share prompts among classes and conduct multi-class anomaly detection.

We aim not only to include the prompt as model input, but also to adjust the original CLIP’s representation to anomaly detection through deep prompting at each layer [10, 11, 29]. Thus, we concatenate  $\mathbf{P}_j^t$  with the output of the previous layer as follows:

$$\mathbf{w}_j = [-, \mathbf{e}_j] = E_T([\mathbf{P}_j^t, \mathbf{e}_{j-1}]) \quad j = 1, \dots, J, \quad (3)$$

where  $J$  denotes the number of prompting layers. For visual encoder  $E_V$ , patch embeddings  $\mathbf{z} = [\mathbf{z}^0, \mathbf{z}^1, \dots, \mathbf{z}^n]$  of an image  $I$  is fed into  $E_V$  as an input. Here,  $\mathbf{z}^0$  refers to the [CLS] token, which retains global-level representation of the image. For visual prompting, we concatenate  $\mathbf{z}_0$  and learnable visual context vector  $\mathbf{P}_0^v \in \mathbb{R}^{C_v \times d_v}$  where  $C_v, d_v$  indicates the visual context length and hidden dimension of  $E_V$ , as an input to  $E_V$ :

$$\mathbf{V}_0^+ = [\mathbf{P}_0^v, \mathbf{z}_0^+], \quad \mathbf{V}_0^- = [\mathbf{P}_0^v, \mathbf{z}_0^-], \quad (4)$$

where  $\mathbf{V}_0^+$  and  $\mathbf{V}_0^-$  indicates visual features for simulated abnormal image  $I^-$  and normal image  $I^+$ . Visual branch performs deep prompting across multiple layers in the same manner as the textual branch.

### 3.2.2 Bidirectional Coupling of Multi-Modal Prompts

Since we do not provide the knowledge on abnormalities with a anomaly-descriptive textual prompts or true abnormal images, prompt learning form a single modality may fail to convey well-aligned representations for anomaly detection. Thus, we design our learnable prompts  $\mathbf{P}^t, \mathbf{P}^v$  to communicate each other. Several works [11, 27] have proposed prompt learning methods that encourage uni-directional communications for image classification; text-to-image [11] and image-to-text [27]. Such an uni-directional propagation of context vectors may result in suboptimal outcomes in anomaly detection when limited amount of images and minimal anomaly cues are available.

Thus, we propose a prompt learning approach that enables bi-directional communication among prompts. To achieve this, we introduce a linear projection for each modality:  $f_{v \rightarrow t} \in \mathbb{R}^{d_v \times d_t}$  and  $f_{t \rightarrow v} \in \mathbb{R}^{d_t \times d_v}$ . Using these projections, we project the prompts  $\mathbf{P}^t$  and  $\mathbf{P}^v$  to each other’s hidden dimensions, obtaining  $\mathbf{P}_0^{t \rightarrow v}$  and  $\mathbf{P}_0^{v \rightarrow t}$ . Consequently, in each layer of both modalities, context vectors are propagated as follows:

$$[-, \rightarrow, \mathbf{w}_j] = E_T([\mathbf{P}_j^t, \mathbf{P}_j^{v \rightarrow t}, \mathbf{w}_{j-1}]), \quad j = 1, \dots, J, \quad (5)$$

$$[-, \rightarrow, \mathbf{z}_j] = E_V([\mathbf{P}_j^v, \mathbf{P}_j^{t \rightarrow v}, \mathbf{z}_{j-1}]), \quad j = 1, \dots, J, \quad (6)$$

## 3.3. Bootstrapping local semantics from CLIP

### 3.3.1 Multi-View Aware Decoder

CLIP is designed to align global-level representations, making it difficult to capture local semantics. AnOPLe modifies internal visual representations through visual prompting, which does not guarantee that V-V attention still extracts enriched local semantics. Therefore, similar to MaskCLIP [26], we introduce a shallow decoder  $D$  to refine the prompted patch tokens and generate a precise anomaly map. The shallow decoder  $D$  consists of three convolution layers (Fig. 2). The patch embedding  $\mathbf{z}[1 : ] \in \mathbb{R}^{n \times d_v}$  of  $I$ , where  $n$  is the number of patches, is upsampled to  $\mathbf{F} \in \mathbb{R}^{h \times w \times d_v}$  via bi-linear interpolation. The convolution layers in  $D$  operate as a channel and spatial mixer, refining the visual representation and mapping it to the textual dimension  $d_t$ .

### 3.3.2 Multi-View Signal $c$

Additionally, to ensure the decoder better learns fine-grained semantics, we feed  $N$  crops  $\{I_i \mid 1 \leq i \leq N\}$  of the original image  $I_0$  along with  $I_0$ . During inference, we only feed  $I_0$  to the model to prevent increased computational costs from processing sub-images. This might cause a distributional shift, making the model overly sensitive to local details while diminishing its ability to perceive the whole image. To address this, we introduce a multi-view signal  $c \in \mathbb{R}^{(N+1) \times d_v}$ . Before being fed into

$E_V$ , each image is mapped to each position  $i$  in  $c$ , where  $1 \leq i \leq N + 1$ .  $c_{N+1}$  corresponds to the entire image. The matched  $c_i$  is prepended to learnable visual context vectors. Although each scale is conditioned on  $c_i$ , sub-images and the entire image share the prompt  $\mathbf{p}^v$ , meaning the context vectors learn local- and global-level knowledge simultaneously. During the test phase, the encoder  $E_V$  and  $\mathbf{p}^v$  only see the original image  $I_0$  conditioned on  $c_{N+1}$ .

### 3.4. Loss Function

#### 3.4.1 Pixel-level Anomaly Detection

For pixel level, we compute loss with predicted pixel-level logits  $\hat{\mathbf{M}} = \langle D(\mathbf{z}), \mathbf{w} \rangle$  and the simulated ground truth mask  $\mathbf{M}$ . The pixel-level loss  $\mathcal{L}_{pixel}$  is defined as

$$\mathcal{L}_{pixel} = \mathcal{L}_{dice}(\langle D(\mathbf{z}), \mathbf{w} \rangle, \mathbf{M}) + \mathcal{L}_{focal}(\langle D(\mathbf{z}), \mathbf{w} \rangle, \mathbf{M}), \quad (7)$$

where  $\mathcal{L}_{dice}$  is a dice loss [21] and  $\mathcal{L}_{focal}$  is a focal loss [15].  $\mathcal{L}_{dice}$  measures the intersections between  $\hat{\mathbf{M}}$  and  $\mathbf{M}$ . Since anomalous pixels occur less frequently than normal pixels, we compute  $\mathcal{L}_{focal}$  to address this imbalance, alongside  $\mathcal{L}_{dice}$ .

#### 3.4.2 Image-level Anomaly Detection

At the image level, we repel negative pairs (normal images and abnormal text embeddings, or vice versa) and attract positive pairs using cross entropy loss  $\mathcal{L}_{ce}$ . The predicted probability of a sample  $I$  being normal or abnormal is defined as follows:

$$\hat{p} = p(y = i|I) = \frac{\exp(\langle \mathbf{z}^{i,0}, \mathbf{w}^i / \tau \rangle)}{\sum_{i \in \{-,+\}} \exp(\langle \mathbf{z}^{i,0}, \mathbf{w}^i / \tau \rangle)}, \quad (8)$$

where  $i$  indicates whether  $I$  is abnormal(-) or normal(+). When computing  $\mathbf{w}$ , we average outputs from all classes within datasets [8]. Next, we compute  $\mathcal{L}_{ce}$  for the predicted probability  $\hat{p} = p(y = i|x)$  for both latent and image perturbations. The resulting image-level loss is defined as:

$$\mathcal{L}_{img} = \mathcal{L}_{ce}(\mathbf{z}^+, \mathbf{z}^-, \mathbf{w}) + \mathcal{L}_{ce}(\mathbf{z}^+, \mathbf{z}_{latent}^-, \mathbf{w}), \quad (9)$$

where  $\mathbf{z}_{latent}^- = \mathbf{z}^+ + \epsilon$  with  $\epsilon \sim N(\mu, \sigma^2)$  is a simulated anomaly with perturbation in the latent space, and  $\mathbf{z}^-$  represents a simulated anomaly in the pixel space. In practice, we apply label smoothing with a smoothing parameter of 0.003 to the latent anomalies.

### 3.4.3 Alignment between Local and Global Semantics

We introduce an additional loss term,  $\mathcal{L}_{align}$ , to align global semantics with local semantics. Since an image is often treated as a bag of patches, local semantics can be beneficial in capturing image-level representations. Moreover, in anomaly detection, image-level anomalies are typically determined based on pixel-level anomalies [6, 18, 22]. Therefore, it is reasonable to utilize local semantics to inform global semantics in order to improve image-level anomaly detection.

However, given that anomalous pixels constitute a small portion of the image, it is risky to take a mere average of pixel-level representation for distillation. Hence, we aggregate pixel-level representations to align with textual semantics (i.e., ‘‘abnormal’’). To achieve this, we multiply the pixel-level logits  $\hat{\mathbf{M}}$  with  $D(\mathbf{z})$  element-wise to obtain  $\mathbf{s} \in \mathbb{R}^{d_v}$  as follows:

$$\mathbf{s} = \sum_{(i,j) \in \{h,w\}} \hat{\mathbf{M}}_{ij} \circ D_{ij}(\mathbf{z}), \quad (10)$$

where  $\hat{\mathbf{M}}_{ij}$  and  $D_{ij}(\mathbf{z})$  refer to the values at  $(i, j)$  of the pixel-level logits and decoder output, respectively. For distillation, we calculate the cosine similarity and subtract it from 1, resulting  $\mathcal{L}_{align} = 1 - \langle \mathbf{z}^0, \mathbf{s} \rangle$ . The final loss is then computed as:

$$\mathcal{L} = \mathcal{L}_{pixel} + \mathcal{L}_{img} + \mathcal{L}_{align}. \quad (11)$$

### 3.5. Anomaly Detection

To determine pixel-level anomalies, we compute an anomaly map  $\mathbf{M}_q \in \mathbb{R}^{h \times w}$  for the query image  $I_q$  as follows:

$$\mathbf{M}_q = 1.0 / ((1.0 / \hat{\mathbf{M}}_q) + (1.0 / \mathbf{M}_{mem})) \in \mathbb{R}^{h \times w}, \quad (12)$$

where  $\hat{\mathbf{M}}_q$  is output of the decoder  $D$ , and  $\mathbf{M}_{mem}$  is a visual memory assisted anomaly map.

To provide details for  $\mathbf{M}_{mem}$ , following [8, 13], we acquire patch features from the  $i$ -th layer of  $E_V$  and store them in the visual memory  $\mathbf{R}$ . At inference time, patch features  $\mathbf{F} \in \mathbb{R}^{h \times w \times d_v}$  from the  $i$ -th layer of query images are compared with  $\mathbf{R}$ .  $\mathbf{M}_{mem} \in [0, 1]^{h \times w}$  is obtained as

$$\mathbf{M}_{mem}^{ij} = \min_{\mathbf{r} \in \mathbf{R}} \frac{1}{2} (1 - \langle \mathbf{F}_{ij}, \mathbf{r} \rangle). \quad (13)$$

Following [8], we aggregate two anomaly maps with harmonic mean. Hence, a image-level anomaly score is computed as

$$score = 1.0 / ((1.0 / \hat{p}) + (1.0 / \max \mathbf{M}_q)). \quad (14)$$

Table 1. **Image- and Pixel-level AUROC performance comparison of anomaly detection on the MVTec and VisA benchmarks.** The highest is highlighted in bold. **Methods relying on prior knowledge of true anomalies are shaded in gray.** Methods using CLIP are marked with a † symbol.

| Method                | Multi-class | Few-shot transfer | MVTec       |          |          |                 |                 |             | VisA            |                 |                 |                 |                 |                 |
|-----------------------|-------------|-------------------|-------------|----------|----------|-----------------|-----------------|-------------|-----------------|-----------------|-----------------|-----------------|-----------------|-----------------|
|                       |             |                   | Image-AUROC |          |          | Pixel-AUROC     |                 |             | Image-AUROC     |                 |                 | Pixel-AUROC     |                 |                 |
|                       |             |                   | 1-shot      | 2-shot   | 4-shot   | 1-shot          | 2-shot          | 4-shot      | 1-shot          | 2-shot          | 4-shot          | 1-shot          | 2-shot          | 4-shot          |
| SPADE                 | ✗           | ✗                 | 81.0±2.0    | 82.9±2.6 | 84.8±2.5 | 91.2±0.4        | 92.0±0.3        | 92.7±0.3    | 79.5±4.0        | 80.7±5.0        | 81.7±3.4        | 95.6±0.4        | 96.2±0.4        | 96.6±0.3        |
| PaDiM                 | ✗           | ✗                 | 76.6±3.1    | 78.9±3.1 | 80.4±2.4 | 89.3±0.9        | 91.3±0.7        | 92.6±0.7    | 62.8±5.4        | 67.4±5.1        | 72.8±2.9        | 89.9±0.8        | 92.0±0.7        | 93.2±0.5        |
| PatchCore             | ✗           | ✗                 | 83.4±3.0    | 86.3±3.3 | 88.8±2.6 | 92.0±1.0        | 93.3±0.6        | 94.3±0.5    | 79.9±2.9        | 81.6±4.0        | 85.3±2.1        | 95.4±0.6        | 96.1±0.5        | 96.8±0.3        |
| RegAD                 | ✓           | ✓                 | -           | 85.7     | 88.2     | -               | 94.6            | 95.8        | -               | -               | -               | -               | -               | -               |
| FastRecon             | ✗           | ✗                 | -           | 91.0     | 94.2     | -               | 95.9            | <b>97.0</b> | -               | -               | -               | -               | -               | -               |
| WinCLIP†              | ✗           | ✗                 | 93.1±2.0    | 94.4±1.3 | 95.2±1.3 | 95.2±0.5        | 96.0±0.3        | 96.2±0.3    | 83.8±4.0        | 84.6±2.4        | 87.3±1.8        | 96.4±0.4        | 96.8±0.3        | 97.2±0.2        |
| AnomalyGPT            | ✓           | ✓                 | 94.1±1.1    | 95.5±0.8 | 96.3±0.3 | 95.3±0.1        | 95.6±0.2        | 96.2±0.1    | <b>87.4±0.8</b> | <b>88.6±0.7</b> | <b>90.6±0.7</b> | 96.2±0.1        | 96.4±0.1        | 96.7±0.1        |
| InCTRL                | ✗           | ✓                 | -           | 94.0±1.5 | 94.5±1.8 | -               | -               | -           | -               | 85.8±2.2        | 87.7±1.9        | -               | -               | -               |
| PromptAD†             | ✗           | ✗                 | 94.6±1.7    | 95.7±1.5 | 96.6±0.9 | <b>95.9±0.5</b> | <b>96.2±0.3</b> | 96.5±0.2    | 86.9±2.3        | 88.3±2.0        | 89.1±1.7        | <b>96.7±0.4</b> | <b>97.1±0.3</b> | <b>97.4±0.3</b> |
| <b>AnoPLe (Ours)†</b> | ✓           | ✗                 | 94.1±2.1    | 95.3±1.9 | 96.3±0.9 | 95.3±0.6        | 95.8±0.5        | 96.3±0.6    | 86.2±2.0        | 86.6±2.6        | 87.7±1.8        | 95.8±0.6        | 95.9±0.6        | 96.5±0.4        |

## 4. Experiments

### 4.1. Datasets

Our experiments utilize the MVTec-AD and VisA datasets, both widely recognized benchmarks in the anomaly detection domain. MVTec-AD comprises high-resolution images from 15 object and texture categories, including surface defects (e.g., scratches, dents) and structural defects (e.g., missing parts), making it a representative benchmark for evaluating anomaly detection models. The VisA dataset, which is more complex than MVTec-AD, contains 10,821 high-resolution images—9,621 normal and 1,200 anomalous—spanning 12 objects characterized by intricate structures, single and multiple instances.

### 4.2. Implementation Details

We use CLIP with a ViT-B/16+ architecture as the backbone, following previous approaches [8],[13]. We train our method for 60 epochs, with the learning rate set to 0.001 for the prompt learner and 0.0002 for the decoder. To generate subimages, we resize images to 480 × 480 pixels and divide them into four non-overlapping crops, while the original image is resized to 240 × 240 pixels. The prompt depth is set to 9, with visual and textual context lengths of 3 for MVTec-AD, and 5 and 8 for VisA.

### 4.3. Evaluation Metrics

We report the Area Under the Receiver Operation Characteristic (AUROC) following the literature [1] for both image- pixel-level anomaly detection.

### 4.4. Main Results

Table 1 shows that our method outperforms baselines (row 1-5) blind to true anomalies by a significant margin (> 10% on MVTec and > 6% on VisA at the image level compared to [18]). Even when compared to methods that assume prior access to true anomalies, our approach remains competitive. For instance, AnoPLe demonstrates superior image-

level performance compared to WinCLIP [8], which uses manually predefined text prompts, in the 1-/ 2-/ 4-shot settings, with improvements of 1.0%/ 0.9%/ 1.1% on MVTec and 2.4%/ 2.0%/ 0.4% on VisA, respectively. We also surpass InCTRL [30], which trains on anomalous samples, across both benchmarks. Additionally, the performance gap between our method and state-of-the-art methods such as AnomalyGPT and PromptAD is minimal—less than 0.5% on MVTec and around 1-2% on VisA in Image and Pixel AUROC.

The slightly larger gap between our method and AnomalyGPT on VisA, compared to MVTec, likely stems from AnomalyGPT being based on large language models (LLMs), which offer more enriched knowledge than CLIP. Furthermore, AnomalyGPT is trained on thousands of normal images and then performs few-shot transfer to other datasets, which allows the model already to be well-prepared with the representations for anomaly detection in the few-shot transfer phase. Nevertheless, given that these SoTA methods rely on explicit anomaly annotations in their text prompts, while our approach does not utilize any anomaly information, this performance gap is reasonable. Additionally, since our model employs highly generic prompts and learns all classes simultaneously rather than with class-specific models, the small gap in AUROC is further justified.

### 4.5. Results on Prompt-guided Anomaly Detection

In Table 2, we present the results of a comparative study on prompt-guided anomaly detection without the assistance of visual memory. We compare our method to PromptAD (using generic prompts, denoted as PromptAD-g, and the original PromptAD with class-specific prompts) and MaPLe with simulated anomalies following DRAEM.

We first compare our method with those that do not use prior knowledge of true anomalies. Even with only generic prompts, our method outperforms the baselines. PromptAD-g experiences a significant drop in AUROC

compared to PromptAD (91.3→81.5), suggesting that textual prompts alone are suboptimal unless paired with anomaly annotations. We also observe that incorporating visual information from pseudo anomalies is beneficial for image-level detection (as seen in MaPLE+DRAEM compared to PromptAD-g). However, naive multi-modal prompting struggles with pixel-level anomaly detection. In contrast, our method captures superior contextual information through prompt learning based on strong cross-modal interactions and a multi-view aware decoder.

Furthermore, despite of being completely blind to true anomalies during training, our method demonstrates competitive results against PromptAD on both benchmarks. Notably, when we extend our model to a per-class approach (AnoPLE\*), it surpasses PromptAD in image-level anomaly detection. While AnoPLE\* slightly lags behind in pixel-level detection on MVTec, it excels on the VisA. In conclusion, these results demonstrate the robustness of our method, even without prior knowledge of true anomalies.

Table 2. **Prompt-guided Anomaly Detection in one-shot setting.** PromptAD-g denotes PromptAD using only generic prompts and AnoPLE\* denotes AnoPLE with class-specific training. The scores for PromptAD are obtained from [13]. The best and second best scores are in bold and underlined, respectively.

| Method      | MVTec       |             | VisA        |             |
|-------------|-------------|-------------|-------------|-------------|
|             | I-AUROC     | P-AUROC     | I-AUROC     | P-AUROC     |
| MaPLE+DRAEM | 86.2        | 30.0        | 63.6        | 37.9        |
| PromptAD-g  | 81.5        | 83.8        | 72.6        | 85.5        |
| PromptAD    | <u>91.3</u> | <b>92.5</b> | <u>83.2</u> | 91.8        |
| AnoPLE      | 91.1        | <u>90.6</u> | 80.8        | <u>92.6</u> |
| AnoPLE*     | <b>92.3</b> | <u>90.6</u> | <b>84.3</b> | <b>92.7</b> |

#### 4.6. Qualitative Results

Figure 3 presents a qualitative comparison of segmentation maps in the one-shot setting. Compared to other models, which often misclassify normal areas as anomalies or miss true anomalous regions, AnoPLE offers more precise localization maps. For Hazelnut, PromptAD detects the object rather than the anomalies, and WinCLIP only partially captures the anomalous regions. In contrast, AnoPLE accurately segments the anomalous regions with high confidence. For Fryum, WinCLIP captures non-anomalous regions, while PromptAD fails to detect anomalies. Meanwhile, AnoPLE correctly detects the anomalous regions, though with some false-positive pixels.

To confirm that our method performs well not only in pixel-level anomaly detection but also at the image level in a qualitative manner, we visualize features from the MVTec and VisA benchmarks. Properly learned context vectors should align textual and visual features while clearly distinguishing between normal and abnormal samples. As shown in Figure 4, even when trained with a single normal image,

the features are well-aligned across modalities, with a clear separation between normal and abnormal samples.

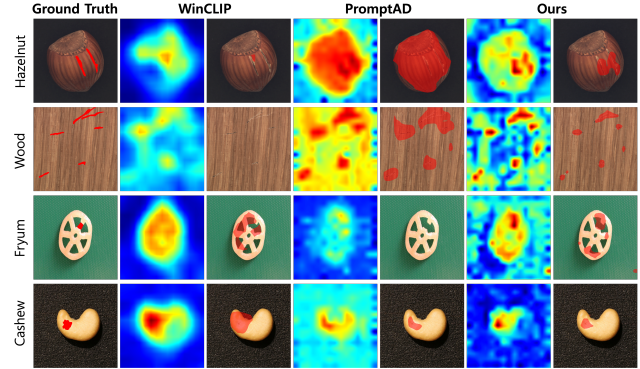


Figure 3. **Qualitative Results on MVTec and VisA for 1-shot Pixel-level Anomaly Detection.** We present heat maps and images highlighted with anomaly regions for each method.

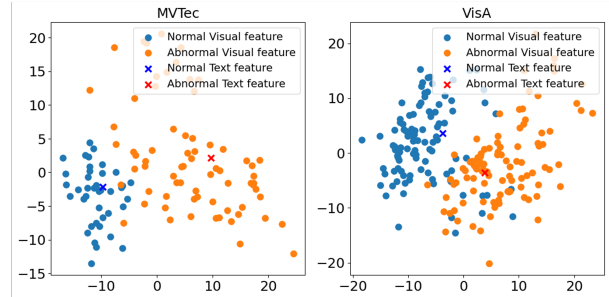


Figure 4. **Image-level Feature Visualization using PCA in a 1-shot setting.** The features “hazelnut” for MVTec and “pcb4” for VisA are used.

#### 4.7. Ablations

##### 4.7.1 Components Analysis

Table 3 presents the ablation results. In Table 3-(a), we compare different interaction settings for context vectors. In MVTec, uni-modal context vectors underperform compared to multi-modal contexts at the image level (83.3, 85.0→87.6, 88.1, 89.3), indicating that uni-modal prompts are suboptimal without prior knowledge of true anomalies. Multi-modal interactions generally improve performance, except when textual prompts are conditioned on visual prompts (row 5). Since visual contexts alone are less effective, we speculate that pseudo anomaly information is less refined when isolated, leading to poorer results (row 2, 5 vs. row 1, 3, 4). Incorporating bi-directional interactions yields the best results, showing that visual information is most effective when tightly integrated with textual information. At the pixel level, visual contexts alone perform similarly to bi-directional prompting. In both MVTec

Table 3. **Ablation Results on MVTec and VisA.** I-AUC and P-AUC refer to Image AUROC and Pixel AUROC, respectively. The best and second-best scores are in bold and underlined, respectively. The last row indicates our default setting.

| Setting       | MVTec       |             | VisA        |             |
|---------------|-------------|-------------|-------------|-------------|
|               | I-AUC       | P-AUC       | I-AUC       | P-AUC       |
| Text          | 85.0        | 88.4        | 77.9        | <b>92.6</b> |
| Image         | 83.3        | 90.6        | 64.0        | 90.4        |
| T & I (indep) | 88.1        | 89.9        | 74.2        | 91.8        |
| T → I         | 89.3        | 90.0        | 75.5        | 90.9        |
| I → T         | 87.6        | 87.2        | 73.9        | 91.1        |
| <b>T ↔ I</b>  | <b>91.1</b> | <b>90.6</b> | <b>80.8</b> | <u>92.5</u> |

| Setting               | MVTec |       | VisA        |             |
|-----------------------|-------|-------|-------------|-------------|
|                       | I-AUC | P-AUC | I-AUC       | P-AUC       |
| multi-scale           | ✗     | ✗     | 83.6        | 87.8        |
| multi-view signal $c$ | ✗     | ✗     | 87.1        | <b>90.8</b> |
| ✓                     | ✓     | ✓     | <u>87.1</u> | <u>90.8</u> |
| ✓                     | ✓     | ✓     | <b>91.1</b> | <u>90.6</u> |

| Setting                        | MVTec       |             | VisA        |             |
|--------------------------------|-------------|-------------|-------------|-------------|
|                                | I-AUC       | P-AUC       | I-AUC       | P-AUC       |
| w/o align loss                 | 89.0        | <b>90.9</b> | 75.8        | <b>93.6</b> |
| align with mean                | 90.4        | <u>90.7</u> | 77.4        | <u>92.7</u> |
| <b>align with weighted sum</b> | <b>91.1</b> | 90.6        | <b>80.8</b> | 92.5        |

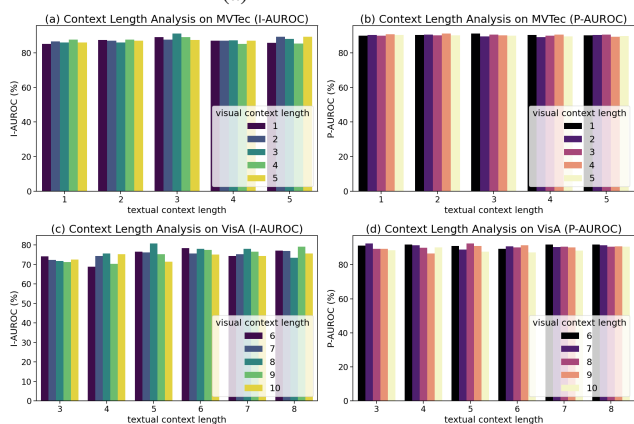


Figure 5. **Comparison Across Different Textual and Visual Context Lengths for MVTec and VisA.**

and VisA, bi-directional coupling achieves the best performance, followed by textual contexts alone. This difference could be due to greater complexity of VisA, where isolated visual information may be more harmful. However, strong inter-modal coupling consistently proves beneficial.

**Table 3-(b)** evaluates the effectiveness of multi-scale training and the multi-view signal  $c$ . Incorporating both local and global views through sub-images enhances both Image and Pixel AUROC, demonstrating benefits not only for pixel-level anomaly detection but also at the image level. In the absence of  $c$ , training with multi-scaled images leads to a significant decrease in I-AUROC, though P-AUROC sees a slight improvement. Finally, **Table 3-(c)** demonstrates the importance of aligning global and local semantics. Aligning global semantics with local features improves anomaly detection performance (row 1 vs. row 2, 3). Additional gains at the image level are observed when global features are aligned with anomaly-aware pixel-level prototypes (i.e., the weighted sum of pixel-level logits in Eq. 10) rather than the merely averaged logits. Aligning both levels of semantics results in a slight reduction in P-AUROC, which is negligible compared to the substantial improvement in I-AUROC.

#### 4.7.2 Analysis on Prompt Lengths

Figure 5 presents our analysis of context length sensitivity. In MVTec, the model shows robust performance in

both image- and pixel-level anomaly detection across different context lengths. The optimal performance occurs when the textual context length is set to 3, and similarly, the visual context length also performs best at 3. In VisA, longer context lengths prove to be more effective than in MVTec, likely due to the increased complexity of the images. As the textual context length increases, it improves image-level anomaly detection. At the pixel level, the model remains robust across various context lengths. However, as the textual context length increases, the model becomes less sensitive to changes in the visual context length. The optimal configuration emerges with 5 and 8 for the textual and visual context length.

## 5. Conclusion

We propose a novel approach for few-shot AD that leverages multi-modal prompt learning with minimal dependence on prior knowledge of anomalies. Our method improves anomaly detection by incorporating bidirectional prompt communication and utilizing a lightweight decoder for precise localization. Experimental results demonstrate that our approach performs comparably in few-shot industrial anomaly detection scenarios, offering an efficient solution for real-world applications. This research sets a new direction for resource-efficient anomaly detection, maintaining high accuracy even with limited training data and without relying on prior knowledge of true anomalies.

## References

- [1] Paul Bergmann, Michael Fauser, David Sattlegger, and Carsten Steger. Mvtec ad—a comprehensive real-world dataset for unsupervised anomaly detection. In *Proceedings of the IEEE/CVF conference on computer vision and pattern recognition*, pages 9592–9600, 2019. 1, 2, 6
- [2] Hanqiu Deng, Zhaoxiang Zhang, Jinan Bao, and Xingyu Li. Anovl: Adapting vision-language models for unified zero-shot anomaly localization. *arXiv preprint arXiv:2308.15939*, 2023. 1, 3
- [3] Choubo Ding, Guansong Pang, and Chunhua Shen. Catching both gray and black swans: Open-set supervised anomaly detection. In *Proceedings of the IEEE/CVF Conference on Computer Vision and Pattern Recognition*, pages 7388–7398, 2022. 1

- [4] Zheng Fang, Xiaoyang Wang, Haocheng Li, Jiejie Liu, Qiguang Hu, and Jimin Xiao. Fastrecon: Few-shot industrial anomaly detection via fast feature reconstruction. In *Proceedings of the IEEE/CVF International Conference on Computer Vision*, pages 17481–17490, 2023. 1
- [5] Zhaopeng Gu, Bingke Zhu, Guibo Zhu, Yingying Chen, Ming Tang, and Jinqiao Wang. Anomalygpt: Detecting industrial anomalies using large vision-language models. In *Proceedings of the AAAI Conference on Artificial Intelligence*, pages 1932–1940, 2024. 2, 3
- [6] Chaoqin Huang, Haoyan Guan, Aofan Jiang, Ya Zhang, Michael Spratling, and Yan-Feng Wang. Registration based few-shot anomaly detection. In *European Conference on Computer Vision*, pages 303–319. Springer, 2022. 1, 2, 5
- [7] Gabriel Ilharco, Mitchell Wortsman, Ross Wightman, Cade Gordon, Nicholas Carlini, Rohan Taori, Achal Dave, Vaishaal Shankar, Hongseok Namkoong, John Miller, Hananeh Hajishirzi, Ali Farhadi, and Ludwig Schmidt. Openclip, 2021. If you use this software, please cite it as below. 1
- [8] Jongheon Jeong, Yang Zou, Taewan Kim, Dongqing Zhang, Avinash Ravichandran, and Onkar Dabeer. Winclip: Zero-/few-shot anomaly classification and segmentation. In *Proceedings of the IEEE/CVF Conference on Computer Vision and Pattern Recognition*, pages 19606–19616, 2023. 1, 2, 5, 6, 3
- [9] Chao Jia, Yinfei Yang, Ye Xia, Yi-Ting Chen, Zarana Parekh, Hieu Pham, Quoc Le, Yun-Hsuan Sung, Zhen Li, and Tom Duerig. Scaling up visual and vision-language representation learning with noisy text supervision. In *International conference on machine learning*, pages 4904–4916. PMLR, 2021. 1, 3
- [10] Menglin Jia, Luming Tang, Bor-Chun Chen, Claire Cardie, Serge Belongie, Bharath Hariharan, and Ser-Nam Lim. Visual prompt tuning. In *European Conference on Computer Vision*, pages 709–727. Springer, 2022. 4, 1
- [11] Muhammad Uzair Khattak, Hanoona Rasheed, Muhammad Maaz, Salman Khan, and Fahad Shahbaz Khan. Maple: Multi-modal prompt learning. In *Proceedings of the IEEE/CVF Conference on Computer Vision and Pattern Recognition*, pages 19113–19122, 2023. 1, 2, 4
- [12] Aodong Li, Chen Qiu, Marius Kloft, Padhraic Smyth, Maja Rudolph, and Stephan Mandt. Zero-shot anomaly detection via batch normalization. *Advances in Neural Information Processing Systems*, 36, 2024. 1
- [13] Xiaofan Li, Zhizhong Zhang, Xin Tan, Chengwei Chen, Yanyun Qu, Yuan Xie, and Lizhuang Ma. Promptad: Learning prompts with only normal samples for few-shot anomaly detection. *arXiv preprint arXiv:2404.05231*, 2024. 1, 2, 3, 5, 6, 7
- [14] Yiting Li, Adam Goodge, Fayao Liu, and Chuan-Sheng Foo. Promptad: Zero-shot anomaly detection using text prompts. In *Proceedings of the IEEE/CVF Winter Conference on Applications of Computer Vision*, pages 1093–1102, 2024. 1
- [15] Tsung-Yi Lin, Priya Goyal, Ross Girshick, Kaiming He, and Piotr Dollár. Focal loss for dense object detection. In *Proceedings of the IEEE international conference on computer vision*, pages 2980–2988, 2017. 5
- [16] Zhikang Liu, Yiming Zhou, Yuansheng Xu, and Zilei Wang. Simplenet: A simple network for image anomaly detection and localization. In *Proceedings of the IEEE/CVF Conference on Computer Vision and Pattern Recognition*, pages 20402–20411, 2023. 3
- [17] Alec Radford, Jong Wook Kim, Chris Hallacy, Aditya Ramesh, Gabriel Goh, Sandhini Agarwal, Girish Sastry, Amanda Askell, Pamela Mishkin, Jack Clark, et al. Learning transferable visual models from natural language supervision. In *International conference on machine learning*, pages 8748–8763. PMLR, 2021. 1, 2, 3
- [18] Karsten Roth, Latha Pemula, Joaquin Zepeda, Bernhard Schölkopf, Thomas Brox, and Peter Gehler. Towards total recall in industrial anomaly detection. In *Proceedings of the IEEE/CVF Conference on Computer Vision and Pattern Recognition*, pages 14318–14328, 2022. 2, 5, 6, 1
- [19] Marco Rudolph, Bastian Wandt, and Bodo Rosenhahn. Same same but different: Semi-supervised defect detection with normalizing flows. In *Proceedings of the IEEE/CVF winter conference on applications of computer vision*, pages 1907–1916, 2021. 1
- [20] Yixuan Su, Tian Lan, Huayang Li, Jialu Xu, Yan Wang, and Deng Cai. Pandagpt: One model to instruction-follow them all. *arXiv preprint arXiv:2305.16355*, 2023. 3
- [21] Carole H Sudre, Wenqi Li, Tom Vercauteren, Sebastien Ourselin, and M Jorge Cardoso. Generalised dice overlap as a deep learning loss function for highly unbalanced segmentations. In *Deep Learning in Medical Image Analysis and Multimodal Learning for Clinical Decision Support: Third International Workshop, DLMIA 2017, and 7th International Workshop, ML-CDS 2017, Held in Conjunction with MICCAI 2017, Québec City, QC, Canada, September 14, Proceedings 3*, pages 240–248. Springer, 2017. 5
- [22] Zhiyuan You, Lei Cui, Yujun Shen, Kai Yang, Xin Lu, Yu Zheng, and Xinyi Le. A unified model for multi-class anomaly detection. *Advances in Neural Information Processing Systems*, 35:4571–4584, 2022. 2, 5
- [23] Vitjan Zavrtanik, Matej Kristan, and Danijel Škočaj. Draem—a discriminatively trained reconstruction embedding for surface anomaly detection. In *Proceedings of the IEEE/CVF International Conference on Computer Vision*, pages 8330–8339, 2021. 1, 2, 3
- [24] Hui Zhang, Zuxuan Wu, Zheng Wang, Zhineng Chen, and Yu-Gang Jiang. Prototypical residual networks for anomaly detection and localization. In *Proceedings of the IEEE/CVF Conference on Computer Vision and Pattern Recognition*, pages 16281–16291, 2023. 1
- [25] Xuan Zhang, Shiyu Li, Xi Li, Ping Huang, Jiulong Shan, and Ting Chen. Destseg: Segmentation guided denoising student-teacher for anomaly detection. In *Proceedings of the IEEE/CVF Conference on Computer Vision and Pattern Recognition*, pages 3914–3923, 2023. 1
- [26] Chong Zhou, Chen Change Loy, and Bo Dai. Extract free dense labels from clip. In *European Conference on Computer Vision*, pages 696–712. Springer, 2022. 2, 4
- [27] Kaiyang Zhou, Jingkang Yang, Chen Change Loy, and Ziwei Liu. Conditional prompt learning for vision-language mod-

- els. In *Proceedings of the IEEE/CVF conference on computer vision and pattern recognition*, pages 16816–16825, 2022. 1, 4
- [28] Kaiyang Zhou, Jingkang Yang, Chen Change Loy, and Ziwei Liu. Learning to prompt for vision-language models. *International Journal of Computer Vision*, 130(9):2337–2348, 2022. 1
- [29] Qihang Zhou, Guansong Pang, Yu Tian, Shibo He, and Jiming Chen. Anomalyclip: Object-agnostic prompt learning for zero-shot anomaly detection. *arXiv preprint arXiv:2310.18961*, 2023. 1, 2, 3, 4
- [30] Jiawen Zhu and Guansong Pang. Toward generalist anomaly detection via in-context residual learning with few-shot sample prompts. *arXiv preprint arXiv:2403.06495*, 2024. 1, 3, 6
- [31] Yang Zou, Jongheon Jeong, Latha Pemula, Dongqing Zhang, and Onkar Dabeer. Spot-the-difference self-supervised pre-training for anomaly detection and segmentation. *arXiv preprint arXiv:2207.14315*, 2022. 1, 2

# AnoPLE: Few-Shot Anomaly Detection via Bi-directional Prompt Learning with Only Normal Samples

## Supplementary Material

### 6. Further Implementation Details

#### 6.1. Data Pre-processing

We normalize our images using CLIP’s pre-computed mean values [0.48145466, 0.4578275, 0.40821073] and standard deviations [0.26862954, 0.26130258, 0.27577711]. During training, in order to generate sub-images, we resize images to  $480 \times 480$  pixels and divide them into four non-overlapping crops, while the original image is resized to  $240 \times 240$  pixels. In a test phase, we feed the model only resized images of  $240 \times 240$  pixels.

#### 6.2. Training Details

We train our model using the SGD optimizer for 60 epochs, with a batch size of 1 and learning rates of 0.001 for the prompt learner and 0.0002 for the decoder. Specifically, we apply a learning rate schedule that warms up from zero to the preset learning rate. For optimizer, we set momentum and weight decay to 0.9 and  $1e-5$ . When computing the alignment loss (Eq. 10), we normalize  $\hat{\mathbf{M}}$  using a temperature-scaled softmax, with the temperature  $\tau$  set to 2. Textual and visual hidden dimension is set to 640 and 896, respectively, following OpenCLIP [7].

#### 6.3. Visual Memory Construction

To provide details for how to obtain visual memory assisted anomaly map, we acquire patch features from the  $i$ -th layer of  $E_V$  and store them in the visual memory  $\mathbf{R}$ , following previous works [8, 13]. At inference time, patch features  $\mathbf{F} \in \mathbb{R}^{h \times w \times d_v}$  from the  $i$ -th layer of query images are compared with  $\mathbf{R}$ . Here,  $h$  and  $w$  are height and width of the image, respectively. The visual memory assisted anomaly score map  $\mathbf{M}_{mem} \in [0, 1]^{h \times w}$  is obtained as  $\mathbf{M}_{ij} = \min_{\mathbf{r} \in \mathbf{R}} \frac{1}{2}(1 - \langle \mathbf{F}_{ij}, \mathbf{r} \rangle)$ . For implementation, we use  $l$  intermediate layers for feature extraction, obtaining  $\mathbf{F} \in \mathbb{R}^{h \times w \times l \times d_v}$  and average them across layers, resulting in  $\mathbf{F} \in \mathbb{R}^{h \times w \times d_v}$ . Specifically, for the MVTec-AD dataset, we extract features from the 7th to 10th layers, while for the VisA dataset, we use the 7th to 9th layers. Following WinCLIP [8] and PromptAD [13], we aggregate prompt-guided and memory-guided anomaly maps with harmonic mean.

#### 6.4. Computational Environments

Our model is trained and evaluated using an NVIDIA A100 80GB GPU and an Intel(R) Xeon(R) Gold 6338 CPU @ 2.00GHz.

### 7. Related Work

We provide additional related work that could not be covered in the main text.

#### 7.1. Anomaly Detection

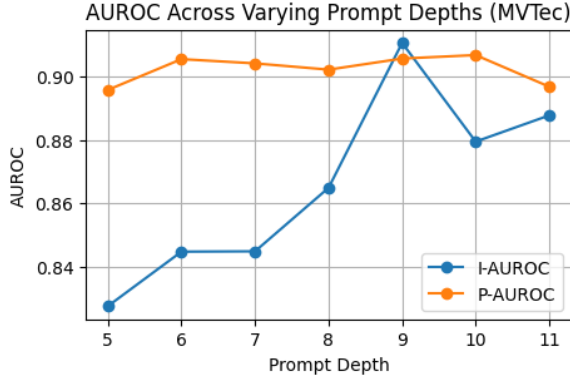
In visual anomaly detection, anomalous samples are rare, leading to the predominance of unsupervised settings. Research in these settings has explored approaches such as reconstruction based methods [23, 25] and feature embedding based approaches [18]. While unsupervised settings are common, there are also studies in supervised settings that include anomalous samples in training [3, 24]. Recently, data efficiency has become a concern, prompting the development of models that generalize well with few or no normal samples. Some studies enable zero-shot anomaly detection [8, 29], performing fully zero-shot domain transfer. Others [12, 14, 29] perform transfer at the class or dataset level similar to traditional image classification domains. In few-shot anomaly detection, methods like [6] align test images with few normal samples, DifferNet [19] is based on normalizing flow, and FastRecon [4] reconstructs anomaly features with distribution regularization.

#### 7.2. Prompt Learning with VLMs

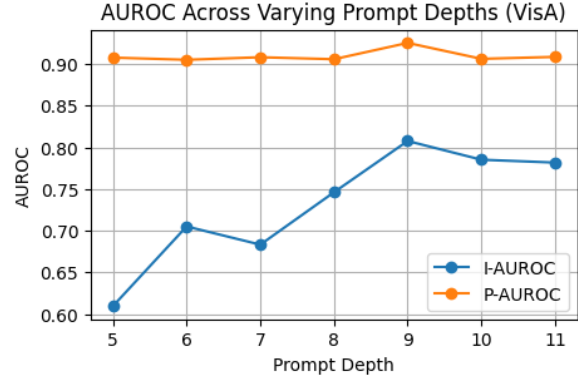
Recently, pre-trained vision-language models (VLMs) such as CLIP [17] have demonstrated high capability in zero- and few-shot image classification. Since updating parameters might cause overfitting or harm their well-learned representation space, prompt learning is preferred over fine-tuning VLMs in few-shot settings. Prompt learning approaches update only the prompts while keeping the weights of the encoder frozen. Pioneering work such as CoOp [28] and CoCoOp [27] has replaced manually engineered textual prompts from CLIP’s text encoder with learnable continuous vectors, achieving strong performance in image classification and domain generalization. VPT [10] has designed learnable visual context vectors for vision-only encoders in multiple layers (deep prompts). Bridging these two, MaPLE [11] performs multi-modal prompt learning by constructing learnable prompts within both the vision and text branches. It outperforms previous uni-modal approaches with the enhanced alignment between two modalities.

### 8. Ablation Studies

We provide additional ablation results. The results are reported without visual memory to fairly evaluate the impact



(a) AUROC across varying prompt depths (MVTec-AD)



(b) AUROC across varying prompt depths (VisA)

Figure 6. Comparison of image and pixel AUROC across different prompt depths for MVTec-AD and VisA datasets.

of each component on AnoPLe. Furthermore, unless otherwise specified, we conduct ablations in the 1-shot setting.

### 8.1. Prompt Depth

Figure 6 presents the results of an ablation study on prompt depth. To ensure a fair evaluation of the effect of prompt depth on performance, we measure both Image and Pixel AUROC without visual memory. In pixel-level detection, the results show greater robustness to changes in prompt depth compared to image-level detection. However, for image-level tasks, AUROC consistently improves as prompt depth increases. The highest performance is achieved when the prompt depth was set to 9, which is our default setting.

### 8.2. Textual Prompt Templates

The input textual prompts for AnoPLe are constructed as follows:

$$\mathbf{e}_0^+ = [\textit{class}], \quad \mathbf{e}_0^- = [\textit{abnormal}][\textit{class}]. \quad (15)$$

We measure the impact of words placed in *[class]* (i.e., class word) and *[abnormal]* (i.e., state word) in Figure 7 and Table 4, respectively.

#### 8.2.1 Ablation on a Class Word.

To examine the impact of the class word on our method, we compare two scenarios: “Object” (following [29]) and “Classname.” In the “Object” scenario, the word “object” is used in place of the class name for all classes, whereas in the “Classname” scenario, the specific class name is inserted into the *[class]* position. As shown in Figure 7, AnoPLe demonstrates greater robustness in pixel-level anomaly detection compared to the image-level. This can be attributed to the ability of decoder to effectively refine the logits from the encoder to better align the localization task. For image-level detection, the results indicate that incorporating class

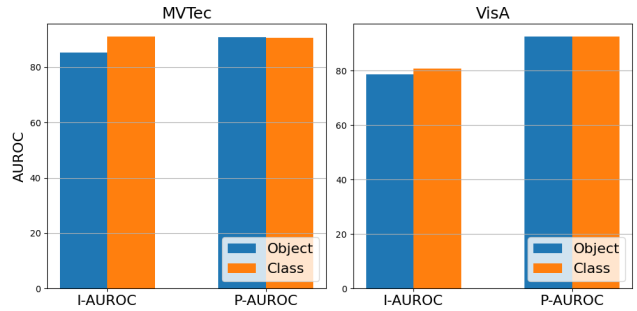


Figure 7. Ablation on the word used in place of *[class]* within the textual prompt. “Object” (colored in blue) uses the word “object” for all classes, while “Class” (colored in orange) represents our default setting, where the specific name of each class is used.

names into the prompt leads to higher AUROC scores. This suggests that leveraging the semantics of class names within the encoder is advantageous for anomaly detection. Given that anomalies often vary across different classes, incorporating class-specific textual information, rather than using a generic “object” term, appears to be a more effective approach for detecting anomalies.

#### 8.2.2 Ablation on a State Word.

We compare several state words (e.g., “damaged,” “anomalous,” “defective”) and the Compositional Prompt Ensemble (CPE) proposed in [8] with our chosen state word, “abnormal.” In the original paper, CPE combines multiple state-level templates with multiple text templates; however, in this ablation, we only use an ensemble of state-level templates. As shown in Table 4, our simple state word, “abnormal,” outperforms or at least competes with other domain-specific options (e.g., “damaged” and “defective”). Although CPE achieves slightly higher AUROC scores at both the image and pixel levels in VisA, it employs a combi-

nation of seven domain-specific words for the normal state and four for the abnormal state. In contrast, AnoPLe leverages a single word—“abnormal”—and competes with CPE on VisA, even outperforming it on MVTec-AD.

Table 4. **Ablation results on state-level templates.** CPE refers to the ensemble of multiple state tokens, using state words as described in [8]. The best scores are in bold, and the second-best are underlined.

| State Tokens      | MVTec-AD    |             | VisA        |             |
|-------------------|-------------|-------------|-------------|-------------|
|                   | I-AUROC     | P-AUROC     | I-AUROC     | P-AUROC     |
| [damaged]         | 90.0        | <u>90.3</u> | 79.7        | <b>93.2</b> |
| [anomalous]       | 88.7        | 89.9        | 79.5        | <u>92.9</u> |
| [defective]       | <u>90.9</u> | 90.0        | 79.6        | 92.7        |
| CPE               | 89.4        | 89.3        | <b>81.2</b> | 92.8        |
| [abnormal] (Ours) | <b>91.1</b> | <b>90.6</b> | <u>80.8</u> | 92.5        |

### 8.3. Anomaly Simulation

Under constraint that we are not able to utilize any cues on true anomalies, whether textual or visual, we simulate anomalies in the pixel and latent space to achieve robust anomaly detection with only few normal images. Specifically, to generate pixel-level pseudo anomalies, we apply Perlin noise to the raw image following DRAEM [23]. For anomaly simulation in the latent space, we follow SimpleNet [16] by adding Gaussian noise to the output of the visual encoder. Table 5 presents the ablation results on the impact of pseudo anomalies at each level on our method. Simulating anomalies in the latent space leads to notably poor performance, indicating that merely adding Gaussian noise to the features of a limited number of normal images fails to provide the model with sufficient signals for anomaly detection. In contrast, using only pixel-level anomalies performs quite well across both datasets. Notably, in MVTec-AD, it slightly outperforms AnoPLe, though the difference is marginal. However, for image-level detection (especially in VisA), the performance remains suboptimal. Overall, the best results are achieved when both levels of pseudo anomalies are used together. While anomaly simulation in the latent space alone is not highly informative, it complements pixel-level pseudo anomalies, resulting in further performance improvements when both are combined.

## 9. Detailed Quantitative Results

Table 6-9 presents class-wise results on the MVTec-AD and VisA benchmarks. We exclude AnomalyGPT [5] from the class-wise comparison since its class-wise results are not reported in the original paper. As shown in Table 6 and 7, we achieve the second-highest scores in most cases on MVTec-AD when averaged across classes. Additionally, following PromptAD [13], we achieve the best performance in the second-highest number of classes. Given that AnoPLe

Table 5. **Ablation results on pseudo anomaly generation in pixel and latent spaces.** The last row indicates our default configuration. The highest scores are indicated in bold, while the second-highest are underlined.

| Pseudo Anomaly |              | MVTec-AD    |             | VisA        |             |
|----------------|--------------|-------------|-------------|-------------|-------------|
| Pixel Space    | Latent Space | I-AUROC     | P-AUROC     | I-AUROC     | P-AUROC     |
| ✗              | ✓            | 56.7        | 73.3        | 59.6        | 66.4        |
| ✓              | ✗            | <u>89.5</u> | <b>90.8</b> | <u>72.7</u> | <u>92.0</u> |
| ✓              | ✓            | <b>91.1</b> | <u>90.6</u> | <b>80.8</b> | <b>92.5</b> |

is trained without access to true anomalies not as previous works[8, 13], this achievement is particularly noteworthy. On the VisA benchmark, we also achieve competitive results compared to the SoTA, with the gap between our method and the SoTA being around 1-2%. In the one-shot setting, this gap even narrows to within 1%.

## 10. Detailed Qualitative Results

### 10.1. Visualization of Anomaly Localization

Figure 9 and 10 present segmentation maps under the 1-shot setting across all classes of the MVTec-AD and VisA datasets. The first, second, third, and fourth columns represent the original image, ground truth, heatmap, and the binary map generated by applying a mask to the binarized heatmap, respectively. Although AnoPLe is trained in a 1-shot setting, it demonstrates the ability to accurately segment anomalies in localized areas across all datasets and classes. Additionally, it shows a tendency to avoid falsely identifying anomalies, resulting in a map that closely resembles the ground truth mask.

### 10.2. Failure Cases

We presents some failure examples in Figure 8 from both MVTec-AD and VisA. The top two rows present examples from the MVTec-AD dataset, while the bottom two rows are from the VisA dataset. The “Cable” case illustrates a scenario where components have been swapped, and the “Transistor” case represents an anomaly caused by the object being misplaced. In such logical anomaly cases, our method fails to accurately localize the anomaly. This can be attributed to the fact that our approach is designed to generate pseudo anomalies for training by creating anomalies at the image-level and pixel-level through noise. As a result, our method is more suited to structural anomalies, showing vulnerability when faced with logical anomalies, as seen in the provided examples. In particular, in the case of “misplaced” objects, the ground truth mask is configured to localize both the correct and incorrect locations, making the ground truth itself ambiguous and difficult to accurately align with the predictions. Additionally, the “Capsules” example from the

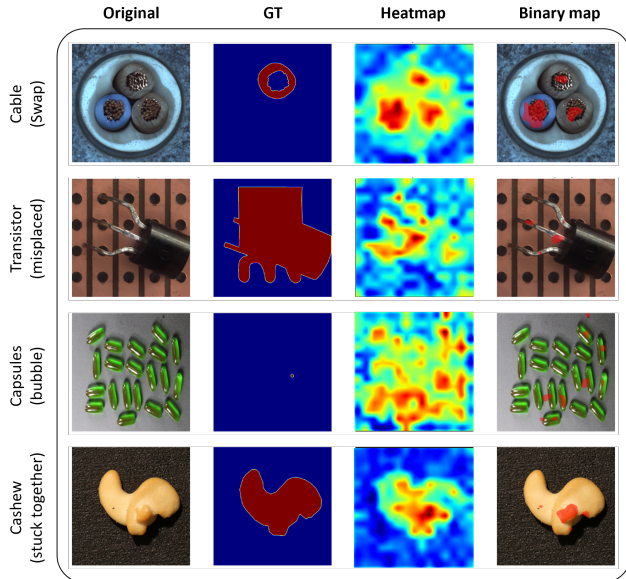


Figure 8. **Failure case on MVTec-AD and VisA.** The top two rows present examples from the MVTec-AD dataset, while the bottom two rows are from the VisA dataset.

VisA dataset illustrates a multi-object image. As seen in the heatmap and binary map, the model not only detects anomalies but also captures multiple objects, highlighting limitations when dealing with such multi-object images. Finally, in the case of “Cashew,” the entire object exhibits a different shape. Our results show that the model focuses more on localizing small defects rather than the overall shape.

### 10.3. Learnable Contexts

AnoPLe encourages active interaction between the two modalities through a bi-directional projection of the learnable context vector, enabling the information in both modalities to complement each other and achieve robust anomaly detection. Our goal is to qualitatively confirm the interaction between the learnable contexts of each modality.

Figure 11 presents the attention matrix corresponding to the positions of the learnable context vectors extracted from AnoPLe for each query image. For MVTec-AD, the first 3 elements in the matrix represent the visual context, while the last 3 represent the textual context. Similarly, for VisA, the first 8 elements correspond to the visual context, and the last 5 correspond to the textual context. Each row of the matrix represents Q in the QKV attention mechanism, while each column represents K. In other words, the rows indicate which parts of the context are being referenced by a given context, and the columns reflect how much a particular context is being attended to by other contexts.

In the early layers (layers 3 and 4), both visual and textual contexts attend to each other in a balanced manner

across the matrix. However, in the middle layers (layers 6-8), the columns associated with the textual context show increased activation, suggesting that both contexts are progressively referencing the textual information. This aligns with a common pattern in Transformer architectures, where earlier layers rely more on local, fine-grained information (e.g., visual). In contrast, later layers shift toward more abstract representations, such as textual context. In contrast to the similar pattern observed in the earlier layers across samples, the later layers of the encoder (layers 10 and 11) reveal two distinct trends: either inter-modal interaction is highly active, or intra-modal interaction dominates (as in the “pcb” and “candle”). However, inter-modal interaction is recovered by the final layer (layer 12).

### 10.4. Multi-view Signal

AnoPLe undergoes multi-scale training by simultaneously learning from sub-images (local view) and full images (global view) during the training phase. However, using sub-images during testing can increase computational load, so only the global view is employed at test time. This difference between the training and testing conditions can introduce a distributional shift. To mitigate this, AnoPLe learns a multi-view signal  $c$  during training, conditioning the model to distinguish between local and global views, which facilitates multi-scale training. During inference, only the global view is used as the condition.

If training is successful, the global view signal is expected to attend to the entire image, similar to how the [CLS] token functions in image classification by focusing on the object as a whole. In contrast, the local view signal is likely to attend to only small portions of the image, potentially failing to capture meaningful semantics. To investigate this, we visualize the attention maps conditioned on both the global and local view signals (Figure 12). For comparison, the attention map of the [CLS] token is also visualized. We visualize attention maps from layer 3.

In Figure 12, the global view signal generally focuses on the object, or in cases where no distinct object is present, it attends to the entire image. Notably, the [CLS] token in AnoPLe, trained to detect abnormalities, not only focuses on the object but also emphasizes anomalous regions in abnormal images. In normal images, both the global view signal and the [CLS] token behave similarly, attending to the object. However, in abnormal images, the [CLS] token specifically highlights the anomalous areas, while the global view signal—without explicit training for abnormality detection—primarily focuses on the object itself. Furthermore, the local view signal often struggles to capture the object and, in the case of “tile”, tends to focus on localized regions rather than the image as a whole.

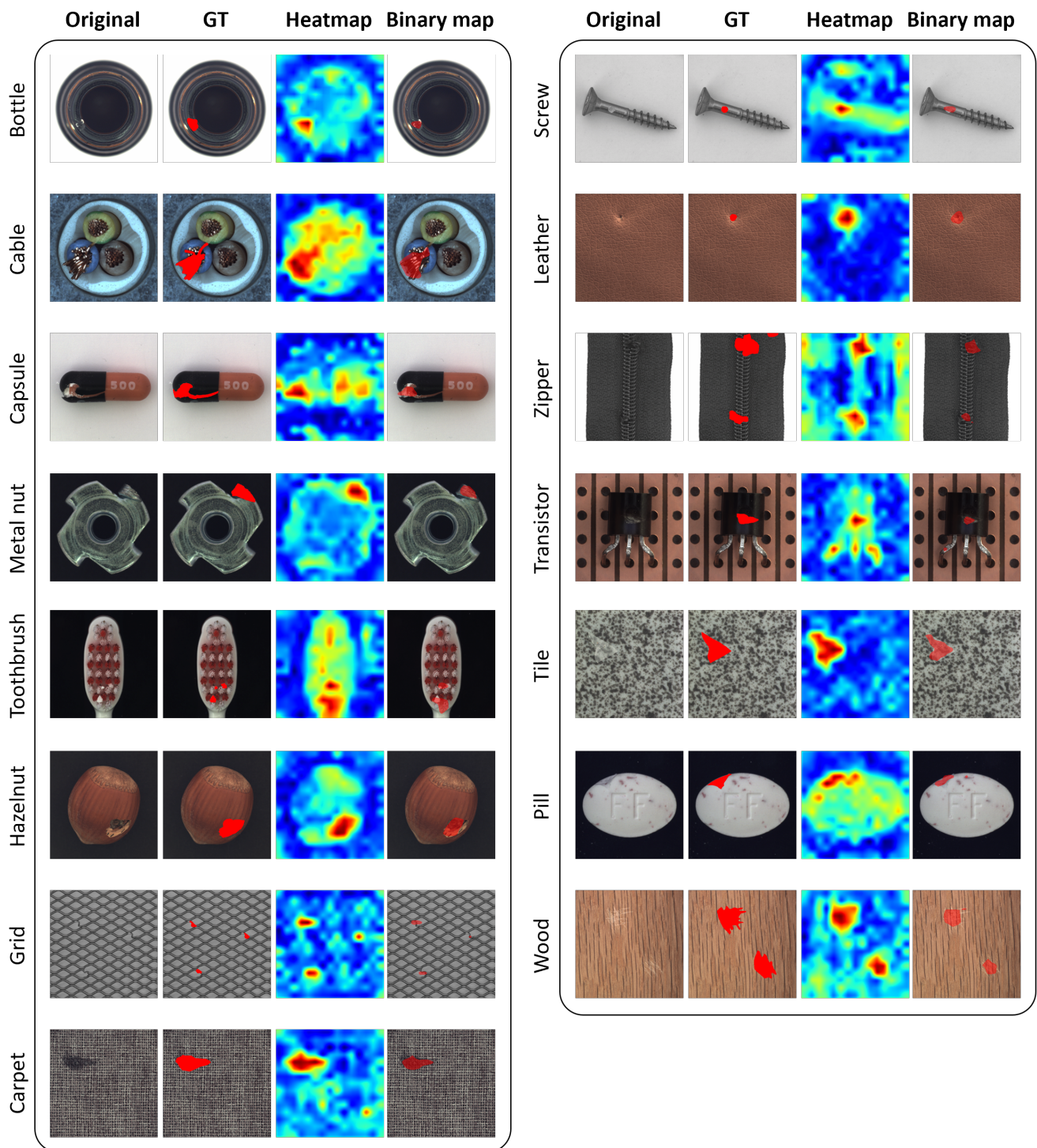


Figure 9. Detailed qualitative results on MVTec-AD from 1-shot AnoPLe.

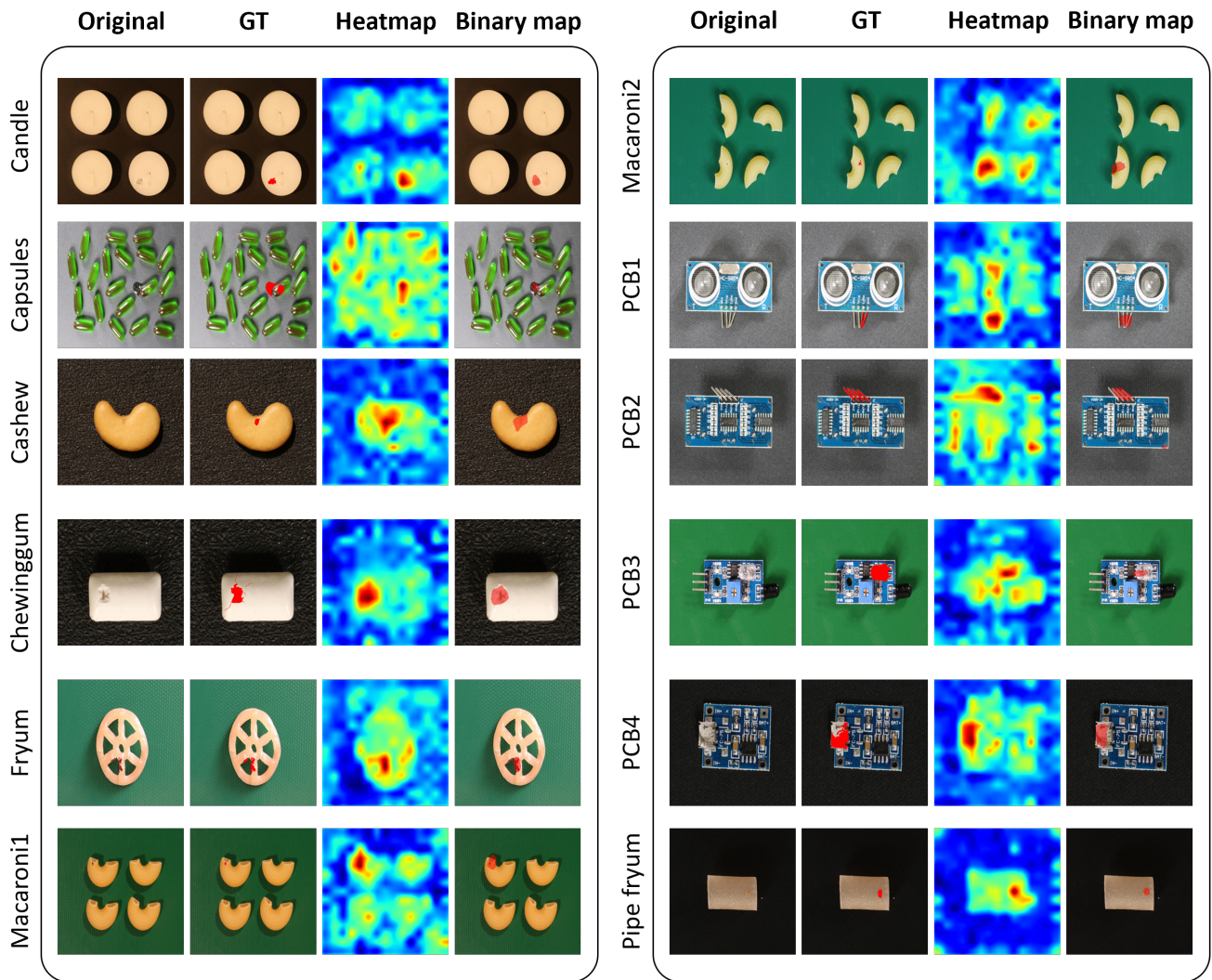


Figure 10. Detailed qualitative results on VisA from 1-shot AnoPLe.

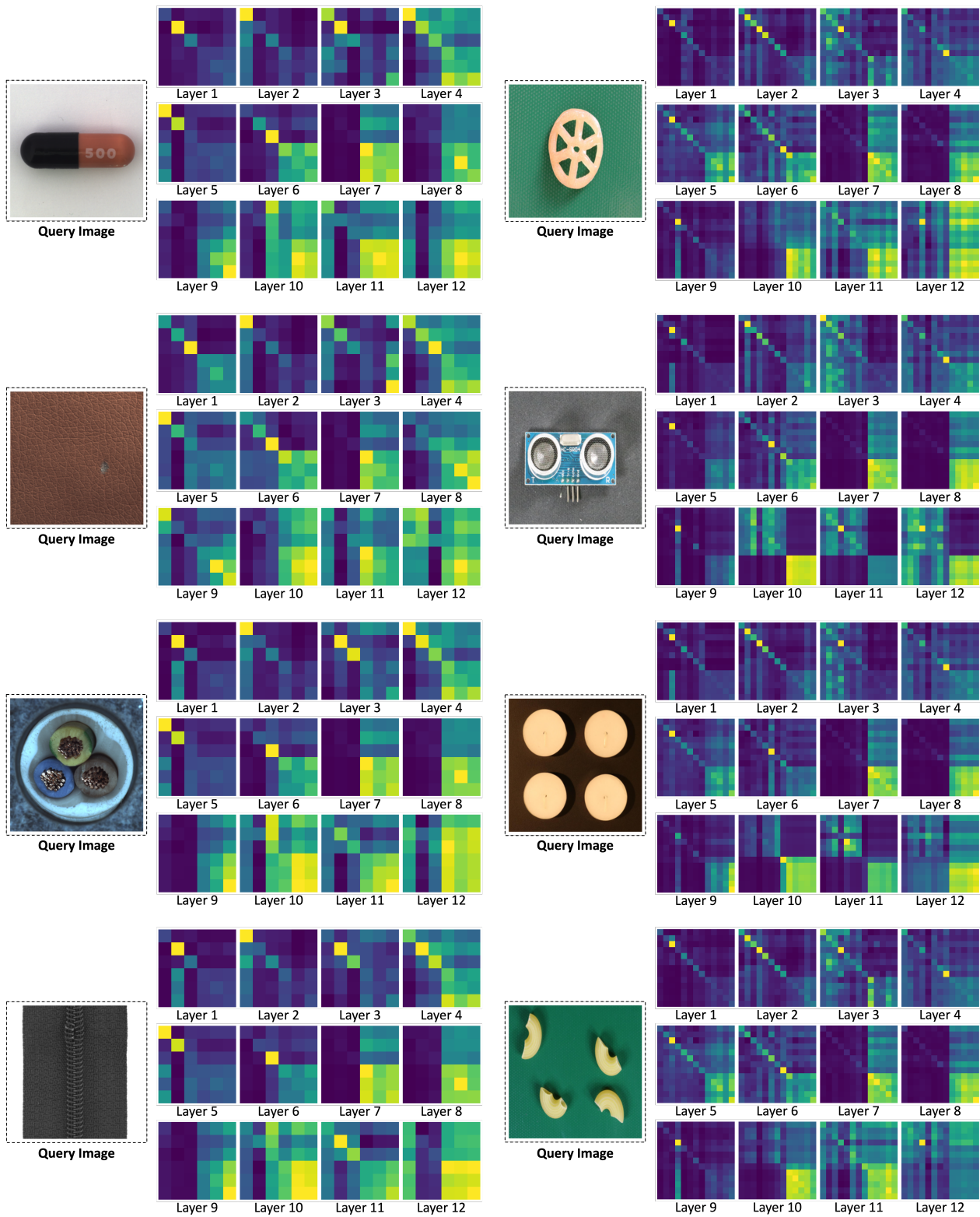


Figure 11. **Attention map visualization of learnable contexts.** The results of the MVTec-AD dataset are presented on the left side, while the results of the VisA dataset are displayed on the right side.

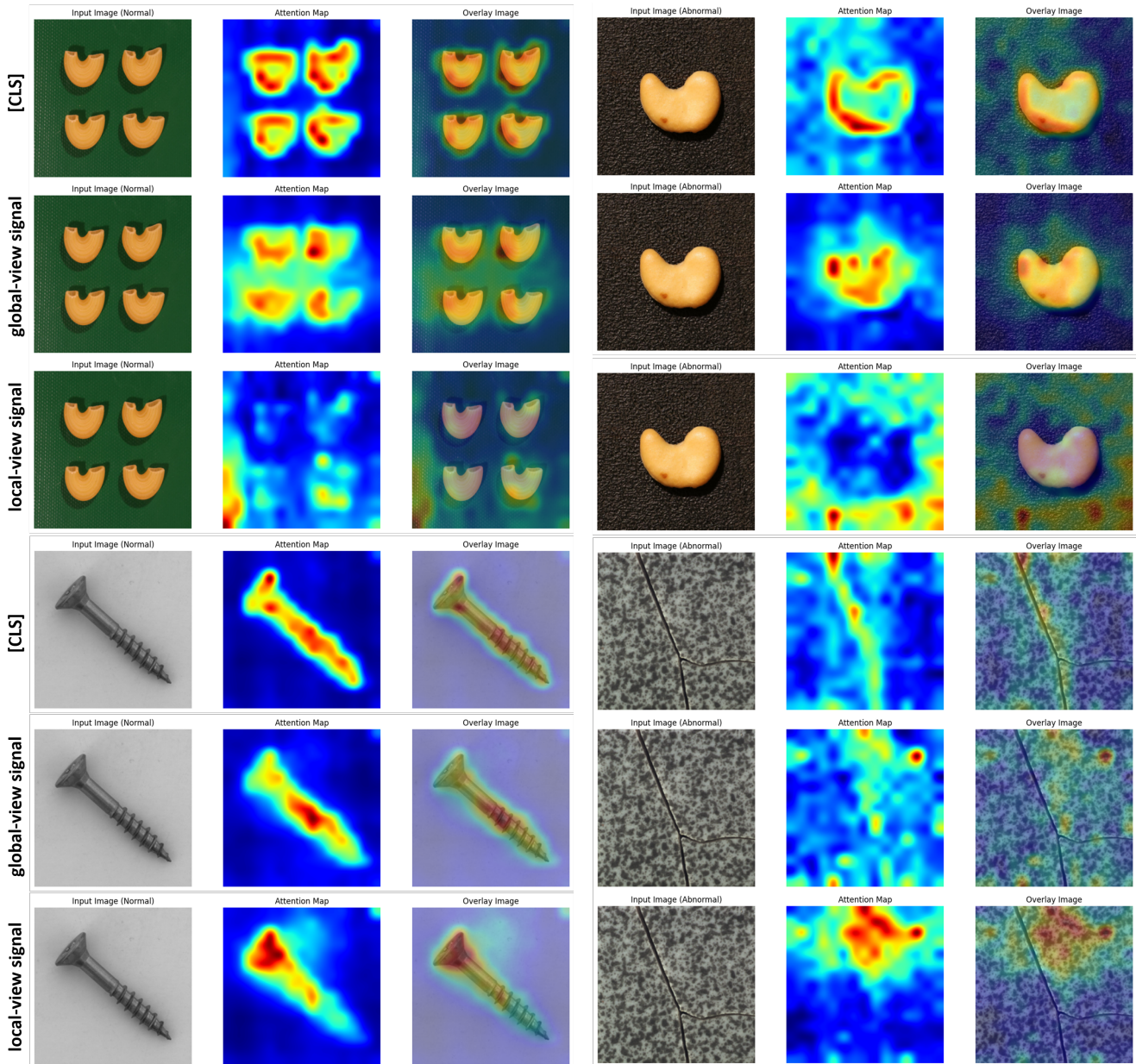


Figure 12. **Comparison of visualized attention maps for multi-view signal.** The first 3 rows present results from the VisA dataset, while the last 3 rows showcase results from the MVTec-AD dataset. The first 3 columns display normal images, and the last 3 columns present abnormal images. Columns 1 and 4 show the original images, columns 2 and 5 display the attention maps, and columns 3 and 6 present the attention overlay images.

Table 6. Comparison of image-level anomaly detection in terms of class-wise AUROC on MVTec-AD. The values in parentheses represent the difference in AUROC between the highest score and our method. Differences within 1.0 are highlighted in red, while those greater than 1.0 are highlighted in blue. The best scores are in bold, and the second-best are underlined.

|            | 1-shot           |           |                 |                  |                       | 2-shot           |           |                 |                  |                       | 4-shot           |                 |                  |                  |                       |
|------------|------------------|-----------|-----------------|------------------|-----------------------|------------------|-----------|-----------------|------------------|-----------------------|------------------|-----------------|------------------|------------------|-----------------------|
|            | SPADE            | PatchCore | WinCLIP+        | PromptAD         | AnoPLe                | SPADE            | PatchCore | WinCLIP+        | PromptAD         | AnoPLe                | SPADE            | PatchCore       | WinCLIP+         | PromptAD         | AnoPLe                |
| Bottle     | 98.7±0.6         | 99.4±0.4  | 98.2±0.9        | <b>99.8±0.3</b>  | 99.2±0.2              | 99.5±0.1         | 99.2±0.3  | 99.3±0.3        | <b>100.0±0.1</b> | 99.6±0.4              | 99.5±0.2         | 99.2±0.3        | 99.3±0.4         | <b>100.0±0.2</b> | 99.9±0.1              |
| Cable      | 71.2±3.3         | 88.8±4.2  | 88.9±1.9        | <b>94.2±1.2</b>  | <u>90.6±2.3</u>       | 76.2±5.2         | 91.0±2.7  | 88.4±0.7        | <b>99.9±1.5</b>  | <u>92.9±1.7</u>       | 83.4±3.1         | 91.0±2.7        | 90.9±0.9         | <b>98.8±0.9</b>  | <u>95.1±1.1</u>       |
| Capsule    | 70.2±3.0         | 67.8±2.9  | 72.3±6.8        | <b>84.6±6.7</b>  | <u>79.4±13.0</u>      | 70.9±6.1         | 72.8±7.0  | 77.3±8.8        | <b>100.0±7.7</b> | <u>85.0±11.5</u>      | 78.9±5.5         | 72.8±7.0        | 82.3±8.9         | <b>100.0±1.5</b> | <u>90.5±2.6</u>       |
| Carpet     | 98.1±0.2         | 95.3±0.8  | 99.8±0.3        | <b>100.0±0.0</b> | <u>99.9±0.1</u>       | 98.3±0.4         | 96.6±0.5  | <b>99.8±0.3</b> | <b>100.0±0.0</b> | <u>99.8±0.1</u>       | 98.6±0.2         | 96.6±0.5        | <b>100.0±0.0</b> | <b>100.0±0.0</b> | <u>99.7±0.2</u>       |
| Grid       | 40.0±6.8         | 63.6±10.3 | 99.5±0.3        | <b>99.8±0.9</b>  | <u>99.7±0.3</u>       | 41.3±3.6         | 67.7±8.3  | <b>99.4±0.2</b> | 98.7±1.2         | <b>99.7±0.5</b>       | 44.6±6.6         | 67.7±8.3        | <u>99.6±0.1</u>  | 98.6±0.5         | <b>99.7±0.2</b>       |
| Hazelnut   | 95.8±1.3         | 88.3±2.7  | 97.5±1.4        | <b>99.8±0.8</b>  | <u>99.6±0.4</u>       | 96.2±2.1         | 93.2±3.8  | 98.3±0.7        | <b>99.4±0.6</b>  | <u>99.4±0.6</u>       | 98.4±1.3         | 93.2±3.8        | 98.4±0.4         | 99.8±0.2         | <b>99.9±0.1</b>       |
| Leather    | <b>100.0±0.0</b> | 97.3±0.7  | <u>99.9±0.0</u> | <b>100.0±0.0</b> | <b>100.0±0.0</b>      | <b>100.0±0.0</b> | 97.9±0.7  | <u>99.9±0.0</u> | 91.8±0.1         | <b>100.0±0.0</b>      | <b>100.0±0.0</b> | <u>97.9±0.7</u> | <b>100.0±0.0</b> | 95.4±0.1         | <b>100.0±0.0</b>      |
| Metal nut  | 71.0±2.2         | 73.4±2.9  | 98.7±0.8        | <b>99.1±0.5</b>  | <b>99.6±0.6</b>       | 77.0±7.9         | 77.7±8.5  | <b>99.4±0.2</b> | 91.3±0.7         | <b>99.5±0.6</b>       | 77.8±5.7         | 77.7±8.5        | <b>99.5±0.2</b>  | 91.5±0.1         | <b>99.5±0.9</b>       |
| Pill       | 86.5±3.1         | 81.9±2.8  | 91.2±2.1        | <b>92.6±1.5</b>  | <b>93.5±1.5</b>       | 84.8±0.9         | 82.9±2.9  | <b>92.3±0.7</b> | <b>100.0±0.8</b> | <u>94.2±0.6</u>       | 86.7±0.3         | 82.9±2.9        | 92.8±1.0         | <b>99.8±0.8</b>  | <u>94.4±0.4</u>       |
| Screw      | 46.7±2.5         | 44.4±4.6  | <b>86.4±0.9</b> | 65.0±2.9         | <u>70.7±5.0</u>       | 46.6±2.2         | 49.0±3.8  | 86.0±2.1        | <b>98.6±2.0</b>  | 76.1±6.8              | 50.5±5.4         | 49.0±3.8        | 87.9±1.2         | <b>100.0±2.3</b> | 79.9±1.6              |
| Tile       | 99.9±0.1         | 99.0±0.9  | <u>99.9±0.0</u> | <b>100.0±0.0</b> | <u>99.4±0.4</u>       | <b>99.9±0.1</b>  | 98.5±1.0  | <b>99.9±0.2</b> | 93.6±0.1         | <u>99.7±0.1</u>       | <b>100.0±0.0</b> | 98.5±1.0        | <u>99.9±0.1</u>  | 92.9±0.1         | <b>99.8±0.2</b>       |
| Toothbrush | 71.7±2.6         | 83.3±3.8  | 92.2±4.9        | <b>98.9±1.0</b>  | <u>97.2±2.0</u>       | 78.6±3.2         | 85.9±3.5  | <b>97.5±1.6</b> | 71.0±1.5         | <u>97.3±1.8</u>       | 78.8±5.2         | 85.9±3.5        | <b>96.7±2.6</b>  | 83.6±0.6         | <b>98.8±2.9</b>       |
| Transistor | 77.2±2.0         | 78.1±6.9  | 83.4±3.8        | <b>94.6±6.5</b>  | <u>89.3±3.5</u>       | 81.3±3.7         | 90.0±4.3  | 85.3±1.7        | <b>97.5±4.0</b>  | <u>91.9±3.4</u>       | 81.4±2.1         | 90.0±4.3        | 85.7±2.5         | <b>98.1±3.8</b>  | <u>93.4±2.5</u>       |
| Wood       | 98.8±0.3         | 99.9±0.3  | <b>99.9±0.1</b> | <b>99.9±0.3</b>  | <u>99.3±0.5</u>       | <b>99.2±0.4</b>  | 98.3±0.6  | <b>99.9±0.1</b> | 97.4±0.1         | <u>99.1±0.7</u>       | 98.9±0.6         | 98.3±0.6        | <b>99.8±0.3</b>  | 95.6±0.3         | <u>99.4±0.1</u>       |
| Zipper     | 89.3±1.9         | 92.3±0.5  | 88.8±5.9        | <u>93.9±3.2</u>  | <b>94.0±1.8</b>       | 93.3±2.9         | 94.0±2.1  | 94.0±1.4        | <b>95.8±1.7</b>  | <u>95.0±0.7</u>       | <b>95.1±1.3</b>  | 94.0±2.1        | 94.5±0.5         | <u>95.0±2.3</u>  | <u>95.0±1.3</u>       |
| Mean       | 81.0±2.0         | 83.4±3.0  | 93.1±2.0        | <b>94.6±1.7</b>  | <u>94.1±2.1 (0.5)</u> | 82.9±2.6         | 86.3±3.3  | 94.4±1.3        | <b>95.7±1.5</b>  | <u>95.3±1.9 (0.4)</u> | 84.8±2.5         | 88.8±2.6        | 95.2±1.3         | <b>96.6±0.9</b>  | <u>96.3±0.9 (0.3)</u> |

Table 7. Comparison of pixel-level anomaly detection in terms of class-wise AUROC on MVTec-AD. The values in parentheses represent the difference in AUROC between the highest score and our method. Differences within 1.0 are highlighted in red, while those greater than 1.0 are highlighted in blue. The best scores are in bold, and the second-best are underlined.

|            | 1-shot          |                 |                 |                 |                       | 2-shot          |                 |                 |                 |                       | 4-shot          |                 |                 |                 |                       |
|------------|-----------------|-----------------|-----------------|-----------------|-----------------------|-----------------|-----------------|-----------------|-----------------|-----------------------|-----------------|-----------------|-----------------|-----------------|-----------------------|
|            | SPADE           | PatchCore       | WinCLIP+        | PromptAD        | AnoPLe                | SPADE           | PatchCore       | WinCLIP+        | PromptAD        | AnoPLe                | SPADE           | PatchCore       | WinCLIP+        | PromptAD        | AnoPLe                |
| Bottle     | 95.3±0.2        | 97.9±0.1        | 97.5±0.2        | <b>99.6±0.2</b> | 97.6±0.3              | 95.7±0.2        | 98.1±0.0        | 97.7±0.1        | <b>99.5±0.1</b> | 97.9±0.0              | 96.1±0.0        | 98.2±0.0        | 97.9±0.0        | <b>99.5±0.1</b> | 97.9±0.1              |
| Cable      | 86.4±0.2        | 95.5±0.8        | 93.8±0.6        | <b>98.4±0.5</b> | 95.4±0.3              | 87.4±0.3        | 96.4±0.3        | 94.3±0.4        | <b>97.6±0.3</b> | 96.0±0.3              | 88.2±0.2        | <u>97.5±0.3</u> | 94.9±0.1        | <b>98.2±0.2</b> | 96.3±0.3              |
| Capsule    | 96.3±0.2        | 95.6±0.4        | 94.6±0.8        | <b>99.5±0.7</b> | 93.8±1.1              | 96.7±0.1        | 96.5±0.4        | 96.4±0.3        | <b>99.3±0.5</b> | 94.2±1.4              | 97.0±0.2        | 96.8±0.6        | 96.2±0.5        | <b>99.3±0.3</b> | 94.9±0.9              |
| Carpet     | 98.2±0.0        | 98.4±0.1        | <b>99.4±0.0</b> | 95.9±0.0        | <u>99.3±0.1</u>       | 98.3±0.0        | 98.5±0.1        | 99.3±0.0        | 96.1±0.0        | 99.2±0.1              | 98.4±0.0        | 98.6±0.1        | <b>99.3±0.0</b> | 96.2±0.0        | 99.2±0.1              |
| Grid       | 80.7±1.3        | 58.8±4.9        | 96.8±1.0        | 95.1±0.5        | <b>98.2±0.2</b>       | 83.5±1.0        | 62.6±3.2        | 97.7±0.8        | 95.5±0.4        | <b>98.2±0.2</b>       | 87.2±1.1        | 69.4±1.3        | 98.0±0.2        | 95.2±0.3        | <b>98.3±0.2</b>       |
| Hazelnut   | 97.2±0.1        | 95.8±0.6        | <b>98.5±0.2</b> | 97.3±0.4        | <u>97.9±0.8</u>       | 97.6±0.1        | 96.3±0.6        | <b>98.7±0.1</b> | 97.6±0.3        | <u>98.3±0.4</u>       | 97.7±0.1        | 97.6±0.1        | <b>98.8±0.0</b> | 97.9±0.2        | <u>98.5±0.1</u>       |
| Leather    | 99.1±0.0        | 98.8±0.2        | <u>99.3±0.0</u> | 93.3±0.0        | <b>99.4±0.0</b>       | 99.1±0.0        | 99.0±0.1        | <u>99.3±0.0</u> | 93.2±0.0        | <b>99.5±0.1</b>       | 99.1±0.0        | 99.1±0.0        | <u>99.3±0.0</u> | 93.9±0.0        | <b>99.4±0.1</b>       |
| Metal nut  | 83.8±0.7        | 89.3±1.4        | <u>90.0±0.6</u> | <b>97.3±0.7</b> | 85.4±0.8              | 85.8±1.1        | 94.6±1.4        | 91.4±0.4        | <b>97.4±0.7</b> | 89.3±1.0              | 87.1±0.7        | 95.9±1.8        | 92.9±0.4        | <b>97.7±0.5</b> | 90.8±1.1              |
| Pill       | 89.4±0.4        | 93.1±1.1        | 96.4±0.3        | <b>98.4±0.4</b> | 95.8±0.2              | 89.9±0.2        | 94.2±0.3        | 97.0±0.2        | <b>98.5±0.3</b> | 96.1±0.2              | 90.7±0.2        | 94.8±0.4        | 97.1±0.0        | <b>98.5±0.2</b> | 96.4±0.2              |
| Screw      | <b>94.8±0.2</b> | 89.6±0.5        | 94.5±0.4        | 91.4±0.5        | 92.6±0.9              | <b>95.6±0.4</b> | 90.0±0.7        | <u>95.2±0.3</u> | 95.1±0.7        | 93.8±0.5              | <b>96.4±0.4</b> | 91.3±1.0        | <u>96.0±0.5</u> | 94.9±0.8        | 95.1±1.0              |
| Tile       | 91.7±0.3        | 94.1±0.5        | <b>96.3±0.2</b> | 92.8±0.1        | <u>96.1±0.7</u>       | 92.0±0.1        | 94.4±0.2        | <b>96.5±0.1</b> | 94.1±0.1        | <u>96.0±0.2</u>       | 92.2±0.1        | 94.6±0.1        | <b>96.6±0.1</b> | 94.1±0.1        | <b>96.7±0.1</b>       |
| Toothbrush | 94.6±0.6        | 97.3±0.4        | 97.8±0.1        | 94.0±0.2        | <b>98.5±0.2</b>       | 96.2±0.3        | 97.5±0.2        | <b>98.1±0.1</b> | 95.5±0.1        | <b>98.5±0.1</b>       | 97.0±0.6        | 98.4±0.4        | 98.4±0.5        | 96.2±0.0        | <b>98.6±0.1</b>       |
| Transistor | 71.4±1.3        | 84.9±2.7        | 85.0±1.8        | <b>99.1±1.9</b> | <u>89.8±1.8</u>       | 72.8±0.9        | 89.6±0.9        | 88.3±1.0        | <b>99.0±1.1</b> | <u>90.7±1.6</u>       | 73.4±0.7        | 90.7±1.4        | 88.5±1.2        | <b>99.0±0.6</b> | <u>92.5±0.7</u>       |
| Wood       | 93.4±0.1        | 92.7±0.9        | 94.6±1.0        | 89.4±0.3        | <b>95.5±0.6</b>       | 93.8±0.1        | 93.2±0.7        | 95.3±0.4        | 89.1±0.2        | <b>95.5±0.6</b>       | 93.9±0.1        | 93.5±0.3        | 95.4±0.2        | 90.6±0.1        | <b>95.6±0.7</b>       |
| Zipper     | 94.9±0.3        | <b>97.4±0.4</b> | 93.9±0.8        | <u>96.6±0.5</u> | <u>92.3±1.1</u>       | <u>95.8±0.2</u> | <b>98.0±0.1</b> | 94.1±0.7        | 95.5±0.4        | 93.2±0.8              | 96.2±0.1        | <b>98.1±0.1</b> | 94.2±0.4        | <u>96.6±0.3</u> | 93.4±0.7              |
| Mean       | 91.2±0.4        | 92.0±1.0        | 95.2±0.5        | <b>95.9±0.5</b> | <u>95.3±0.6 (0.6)</u> | 92.0±0.3        | 93.3±0.6        | 96.0±0.3        | <b>96.2±0.3</b> | <u>95.8±0.5 (0.4)</u> | 92.7±0.3        | 94.3±0.5        | 96.2±0.3        | <b>96.5±0.2</b> | <u>96.3±0.6 (0.2)</u> |

Table 8. Comparison of image-level anomaly detection in terms of class-wise AUROC on VisA. The values in parentheses represent the difference in AUROC between the highest score and our method. Differences within 1.0 are highlighted in red, while those greater than 1.0 are highlighted in blue. The best scores are in bold, and the second-best are underlined.

|              | 1-shot    |                 |                 |                 |                       | 2-shot          |                 |                 |                 |                       | 4-shot          |                 |                 |                 |                       |
|--------------|-----------|-----------------|-----------------|-----------------|-----------------------|-----------------|-----------------|-----------------|-----------------|-----------------------|-----------------|-----------------|-----------------|-----------------|-----------------------|
|              | SPADE     | PatchCore       | WinCLIP+        | PromptAD        | AnoPLe                | SPADE           | PatchCore       | WinCLIP+        | PromptAD        | AnoPLe                | SPADE           | PatchCore       | WinCLIP+        | PromptAD        | AnoPLe                |
| Candle       | 86.1±5.6  | 85.1±1.4        | <b>93.4±1.4</b> | 90.3±2.7        | <u>91.6±1.0</u>       | 91.3±3.3        | 85.3±1.5        | <b>94.8±1.0</b> | 91.0±1.2        | <u>93.2±3.2</u>       | 92.8±2.1        | 87.8±0.8        | <b>95.1±0.3</b> | <u>93.0±1.2</u> | 92.6±2.6              |
| Capsules     | 73.3±7.5  | 60.0±7.6        | <b>85.0±3.1</b> | 84.5±3.5        | 79.8±3.5              | 71.7±11.2       | 57.8±5.4        | <b>84.9±0.8</b> | <u>84.9±3.7</u> | 78.1±3.6              | 73.4±7.1        | 63.4±5.4        | <b>86.8±1.7</b> | <u>80.6±2.1</u> | 78.3±3.8              |
| Cashew       | 95.9±1.1  | 89.5±4.4        | 94.0±0.4        | <b>95.6±1.0</b> | 92.3±1.7              | <b>97.3±1.4</b> | 93.6±0.6        | 94.3±0.5        | <b>94.7±1.4</b> | 91.6±1.3              | <b>96.4±1.3</b> | 93.0±1.5        | <u>95.2±0.8</u> | 93.6±2.2        | 91.7±1.0              |
| Cheewing gum | 92.1±2.0  | <u>97.3±0.3</u> | <b>97.6±0.8</b> | 96.4±1.2        | 96.9±0.7              | 93.4±1.0        | <b>97.8±0.6</b> | <u>97.3±0.8</u> | 96.6±0.6        | 96.8±0.5              | 93.5±1.4        | <b>98.3±0.3</b> | <u>97.7±0.3</u> | 96.8±0.4        | 96.8±0.6              |
| Fryum        | 81.1±4.0  | 75.0±4.8        | 88.5±1.9        | <b>90.3±1.8</b> | 87.5±2.9              | <b>90.5±3.9</b> | 83.4±2.4        | <b>90.5±0.4</b> | 89.2±0.9        | 88.3±2.9              | <b>92.9±1.6</b> | 88.6±1.3        | <u>90.8±0.5</u> | 89.0±2.3        | 90.1±0.9              |
| Macaroni1    | 66.0±10.5 | 68.0±3.4        | 82.9±1.5        | <b>88.6±3.1</b> | 83.5±1.8              | 69.1±8.2        | 75.6±4.6        | 83.3±1.9        | <u>84.2±2.5</u> | <b>84.4±2.3</b>       | 65.8±1.2        | 82.9±2.7        | 85.2±0.9        | <b>88.2±2.5</b> | 87.2±1.9              |
| Macaroni2    | 55.8±6.1  | 55.6±4.6        | <b>70.2±0.9</b> | 69.1±3.0        | 67.8±3.8              | 58.3±4.4        | 57.3±5.6        | 71.8±2.0        | <b>82.6±0.9</b> | 66.7±5.2              | 56.7±3.2        | 61.7±1.8        | 70.9±2.2        | <b>81.2±1.8</b> | 69.7±2.6              |
| PCB1         | 87.2±2.3  | 78.9±1.1        | 75.6±23.0       | <b>88.7±0.7</b> | 87.4±3.0              | 86.7±1.1        | 71.5±20.0       | 76.7±5.2        | <b>90.9±5.4</b> | 89.4±0.6              | 83.4±8.5        | 84.7±6.7        | 88.3±1.7        | <b>90.9±2.5</b> | 89.8±1.3              |
| PCB2         | 73.5±3.7  | <b>81.5±0.8</b> | 62.2±3.9        | 71.6±4.1        | <u>77.0±1.9</u>       | 70.3±8.1        | <b>84.3±1.7</b> | 62.6±3.7        | 73.0±3.0        | 80.6±3.8              | 71.7±7.0        | <b>84.3±1.0</b> | 67.5±2.6        | 78.6±2.5        | 81.0±2.6              |
| PCB3         | 72.2±1.0  | <b>82.7±2.3</b> | 74.1±1.1        | <u>79.1±3.6</u> | 78.6±2.2              | 75.8±5.7        | <b>84.8±1.2</b> | 78.8±1.9        | 76.2±2.2        | <u>79.1±4.2</u>       | 79.0±4.1        | <b>87.0±1.1</b> | 83.3±1.7        | 80.3±1.7        | 82.0±1.7              |
| PCB4         | 93.4±1.3  | <b>93.9±2.8</b> | 85.2±8.9        | 91.4±3.2        | 93.5±1.2              | 86.1±8.2        | <b>94.3±3.2</b> | 82.3±9.9        | <b>97.5±2.4</b> | 92.2±3.0              | 95.4±2.3        | <b>95.6±1.6</b> | 87.6±8.0        | <b>97.8±1.4</b> | 94.3±1.4              |
| Pipe fryum   | 77.9±3.2  | 90.7±1.7        | <u>97.2±1.1</u> | 96.9±0.2        | <b>98.7±0.2</b>       | 78.1±3.0        | 93.5±1.3        | 98.0±0.6        | <b>98.9±0.3</b> | 98.6±0.3              | 79.3±0.9        | 96.4±0.7        | <u>98.5±0.4</u> | <b>98.6±0.2</b> | 98.5±0.6              |
| Mean         | 79.5±4.0  | 79.9±2.9        | 83.8±4.0        | <b>86.9±2.3</b> | <u>86.2±2.0 (0.7)</u> | 80.7±5.0        | 81.6±4.0        | 84.6±2.4        | <b>88.3±2.0</b> | <u>86.6±2.6 (1.7)</u> | 81.7±3.4        | 85.3±2.1        | 87.3±1.8        | <b>89.1±1.7</b> | <u>87.7±1.8 (1.4)</u> |

Table 9. Comparison of pixel-level anomaly detection in terms of class-wise AUROC on VisA. The values in parentheses represent the difference in AUROC between the highest score and our method. Differences within 1.0 are highlighted in red, while those greater than 1.0 are highlighted in blue. The best scores are in bold, and the second-best are underlined.

|  | 1-shot |  |  |  |  | 2-shot |  |  |  |  | 4-shot |  |  |  |  |
|--|--------|--|--|--|--|--------|--|--|--|--|--------|--|--|--|--|
|  |        |  |  |  |  |        |  |  |  |  |        |  |  |  |  |